Astronomy & Astrophysics manuscript no. Frasca˙gvel˙cha˙astroph
December 16, 2014

The Gaia-ESO Survey: Chromospheric Emission, Accretion Properties, and Rotation in γ Velorum and Chamaeleon I⋆,⋆⋆

A. Frasca[1], K. Biazzo[1], A. C. Lanzafame[2,1], J. M. Alcalá[3], E. Brugaletta[2,1], A. Klutsch[1], B. Stelzer[4], G. G. Sacco[5], L. Spina[5], R. D. Jeffries[6], D. Montes[7], E. J. Alfaro[8], G. Barentsen[9], R. Bonito[10,4], J. F. Gameiro[11], J. López-Santiago[12], G. Pace[11], L. Pasquini[13], L. Prisinzano[4], S. G. Sousa[11,14], G. Gilmore[15], S. Randich[5], G. Micela[4], A. Bragaglia[16], E. Flaccomio[4], A. Bayo[17,18], M. T. Costado[8], E. Franciosini[5], V. Hill[19], A. Hourihane[15], P. Jofré[15], C. Lardo[16], E. Maiorca[5], T. Masseron[15], L. Morbidelli[5], and C. C. Worley[15]

(Affiliations can be found after the references)

Received / accepted

ABSTRACT

Aims. One of the scopes of the Gaia-ESO Survey (GES), which is conducted with FLAMES at the VLT, is the census and the characterization of the low-mass members of very young clusters and associations. We conduct a comparative study of the main properties of the sources belonging to γ Velorum (γ Vel) and Chamaeleon I (Cha I) young associations, focusing on their rotation, chromospheric radiative losses, and accretion.

Methods. We use the fundamental parameters (effective temperature, surface gravity, lithium abundance, and radial velocity) delivered by the GES consortium in the first internal data release to select the members of γ Vel and Cha I among the UVES and GIRAFFE spectroscopic observations. A total of 140 γ Vel members and 74 Cha I members were studied. The procedure adopted by the GES to derive stellar fundamental parameters provided also measures of the projected rotational velocity ($v \sin i$). We calculated stellar luminosities through spectral energy distributions, while stellar masses were derived by comparison with evolutionary tracks. The spectral subtraction of low-activity and slowly rotating templates, which are rotationally broadened to match the $v \sin i$ of the targets, enabled us to measure the equivalent widths (EWs) and the fluxes in the Hα and Hβ lines. The Hα line was also used for identifying accreting objects, on the basis of its equivalent width and the width at the 10% of the line peak (10%W), and for evaluating the mass accretion rate ($\dot{M}_{\rm acc}$).

Results. The distribution of $v \sin i$ for the members of γ Vel displays a peak at about 10 km s^{-1} with a tail toward faster rotators. There is also some indication of a different $v \sin i$ distribution for the members of its two kinematical populations. Most of these stars have Hα fluxes corresponding to a saturated activity regime. We find a similar distribution, but with a narrower peak, for Cha I. Only a handful of stars in γ Vel display signatures of accretion, while many more accretors were detected in the younger Cha I, where the highest Hα fluxes are mostly due to accretion, rather than to chromospheric activity. Accreting and active stars occupy two different regions in a $T_{\rm eff}$–flux diagram and we propose a criterion for distinguishing them. We derive $\dot{M}_{\rm acc}$ in the ranges 10^{-11}–$10^{-9} M_\odot$ yr^{-1} and 10^{-10}–$10^{-7} M_\odot$ yr^{-1} for γ Vel and Cha I accretors, respectively. We find less scatter in the $\dot{M}_{\rm acc} - M_\star$ relation derived through the Hα EWs, when compared to the Hα 10%W diagnostics, in agreement with other authors.

Key words. Stars: chromospheres – Accretion – Stars: pre-main sequence/low-mass/rotation – Open clusters and associations: individual: γ Velorum, Chamaeleon I – Techniques: spectroscopic

1. Introduction

During the pre-main sequence (PMS) evolutionary phase, solar-like and low-mass stars undergo remarkable changes of their internal structure, radius, temperature and rotation velocity. Moreover, several phenomena affect their atmospheric layers and circumstellar environments with noticeable effects on the observed spectra.

The rotation velocity distribution of stars in young clusters and associations is a fundamental tool to understand the relative importance of the processes that lead the stars to spin up during their early life (contraction and mass accretion) over those which tend to slow down them (magnetic braking and disk locking). Disks appear to regulate the stellar rotation only for about the first 5 Myr of their life or less, when they are very frequent and detected at infrared wavelengths (e.g., Lada et al. 2006; Sicilia-Aguilar et al. 2006, and references therein) and accretion signatures, like strong and broad emission lines, are seen in the stellar spectra. After 5 Myr the disks dissipate quickly (e.g., Haisch et al. 2001; Hernández et al. 2008) and the stars are free to spin up as they contract and approach the zero-age main-sequence (ZAMS). The disk locking effect has been invoked as the responsible for the bimodal distribution of rotation periods observed in very young clusters for stars with $M > 0.25 M_\odot$ with the slower rotators

Send offprint requests to: A. Frasca

⋆ Based on data products from observations made with ESO Telescopes at the La Silla Paranal Observatory under programme ID 188.B-3002.

⋆⋆ Figures 2–4 and Tables 2–6 are only available in electronic form at `http://www.aanda.org`.

being very often objects with infrared excess from circumstellar disks (e.g., Herbst et al. 2002; Rebull et al. 2002). The presence of both slow and fast rotators is still observed in older clusters and associations with ages from about 30 to 200 Myr (see, e. g., Messina et al. 2003; Meibom et al. 2009; Messina et al. 2010, and references therein) and predicted by the models of angular momentum evolution (e.g., Bouvier et al. 1997; Spada et al. 2011).

The magnetic activity is closely related to the stellar evolution during the PMS and main-sequence (MS) stages, and the resulting changes in the internal structure and surface rotation rate. Indeed, the dynamo mechanism generating the magnetic fields depends on the stellar rotation, differential rotation, and sub-photospheric convection. For stars in the MS phase, the level of magnetic activity, as expressed by the average chromospheric emission (CE), has been shown to decay with age due to magnetic braking, since the pioneering work of Skumanich (1972), who proposed a simple power law of the form CE$\propto t^{-1/2}$. Further works based on stars belonging to clusters and moving groups of different ages have proposed different relations between CE and age (see, e.g., Soderblom et al. 1991; Pace & Pasquini 2004; Mamajek & Hillenbrabd 2008). Recent indications support the CE decline with age till about 2 Gyr and a nearly constant behaviour thereafter (e.g., Pace 2013). The age-activity-rotation relation has been also investigated by means of the X-ray coronal emission (e.g., Pizzolato et al. 2003; Preibisch & Feigelson 2005). However, due to their faintness, very low-mass stars in many open clusters (OCs) and associations were only observed recently.

The picture is more complicated for stars in the PMS phase, when accretion of material from the circumstellar disk onto the central star occurs. In particular, mass accretion in the early PMS evolution is responsible for a significant fraction of the final stellar mass and the time dependence of the mass accretion rate is important to trace the disk evolution and its dissipation, contributing to the conditions for both stellar and planetary formation (e.g., Hartmann 1998). This implies that, during the PMS evolutionary phases, mass accretion affects the spectral diagnostics of CE, and, at the same time, chromospheric activity can be a source of contamination in the measurements of mass accretion rates. The effects of accretion and magnetic activity on the optical emission lines become comparable at the final stages of the PMS evolution and in very low-mass stars (Calvet et al. 2005; Bayo et al. 2012; Ingleby et al. 2013, and references therein). As recently found by Manara et al. (2013) for young disk-less (Class III) stellar objects with spectral types from mid-K to late M, the CE, if misinterpreted as an effect of accretion, would give rise to mass accretion rates ($\dot{M}_{\rm acc}$) ranging from $\sim 6.3\times10^{-10} M_\odot$ yr^{-1} for solar-mass young ($\sim$ 1 Myr) stars to $\sim 2.5\times10^{-12} M_\odot$ yr^{-1} for low-mass older ($\sim$ 10 Myr) objects. These authors consider this as a "noise" that is introduced by the CE or, equivalently, as a threshold for the detection of accretion.

The Gaia-ESO Survey (GES, Gilmore et al. 2012; Randich et al. 2013) offers the possibility to considerably extend the dataset of low-mass PMS stars with intermediate- and high-resolution spectra. Indeed, it is observing with FLAMES@VLT a very large sample ($\sim 10^5$) of stars, surveying also more than 70 OCs and star forming regions (SFRs) of different ages. The large number of members of the nearby SFRs and young OCs surveyed by the GES, besides the chemical composition and kinematics, enables us to make a comparative study of their basic properties like rotation velocity, level of magnetic activity, and incidence of mass accretion, which depend on stellar mass and cluster age.

As suitable laboratories to study the evolution of these parameters during the first 10 Myr, we present here the case of γ Velorum (hereafter γ Vel) and Chamaeleon I (hereafter Cha I), which are the first two young clusters observed within the GES.

γ Vel is a nearby ($\sim$ 350 pc) PMS OC with an age of 5–10 Myr and low extinction (A_V = 0.131 mag, Jeffries et al. 2009). Its members are distributed around the double-lined high-mass spectroscopic binary system γ^2 Vel (Pozzo et al. 2000). It belongs to the Vela OB2 association ($\alpha \sim 8^{\rm h}$, $\delta \sim -47^\circ$), a group of $\sim$ 100 early-type stars spread over an angular diameter of $\sim$ 10 deg (see de Zeeuw et al. 1999). Using the *Spitzer* mid-infrared (MIR) data, Hernández et al. (2008) found a low frequency of circumstellar disks around low-mass stars. Moreover, the IR flux excess in γ Vel is lower than that found in stellar populations with a similar age. They propose that the strong radiation field and winds from the components of the γ^2 Vel binary could be responsible for a relatively fast dissipation of the circumstellar dust around the nearby stars.

The Cha I dark cloud, at a distance of 160 $\pm$ 15 pc (Whittet et al. 1997), is one of the three main clouds of the Chamaeleon complex ($\alpha \sim 12^{\rm h}$, $\delta \sim -78^\circ$). It extends over a few square degrees in the sky and its population consists of 237 known members, including sub-stellar objects (see Luhman 2008 for a recent review). As Cha I is younger than γ Vel (age $\sim$ 2 Myr, Luhman 2008), this age difference allows us to perform a comparative analysis in terms of stellar activity and accretion.

This paper is based on results obtained by the GES on these two clusters in preparation to the first advanced data product release[1]. The GES analysis of spectra in the field of young open clusters is described in Lanzafame et al. (2014), while some aspects relevant to the study of chromospheric activity, accretion and rotation are described in more details here. Furthermore, we present results based on an alternative approach for the analysis of accretion that makes use of the line luminosity and that will be introduced in future GES data releases.

In Sect. 2 we briefly describe the data used in this paper and member selection. In Sect. 3 the analysis of the projected rotation velocity, the veiling, the spectral energy distribution, the Hertzsprung-Russell (HR) diagram, the Hα and Hβ line equivalent widths and fluxes, and the mass accretion rate are reported. The discussion of our results on rotation, chromospheric emission, and accretion diagnostics is given in Sect. 4, while the conclusions are drawn in Sect 5.

2. Data

Our analysis is based on the products of spectroscopy obtained during the first six months of observations which are internally released to the members of the GES consortium in the GESviDR1Final catalog[2].

[1] see http://www.eso.org/sci/observing/phase3/data_releases.html
[2] http://ges.roe.ac.uk/

The target selection has been done according to the GES guidelines for the cluster observations (see, Bragaglia et al. 2014). The observations were performed using the CD#3 cross disperser ($R = 47\,000$, $\lambda = 4764$–6820 Å) for UVES and the HR15N grating setting ($R = 17\,000$, $\lambda = 6445$–6815 Å) for GIRAFFE. A brief observing log is given in Table 1. A total of 1242 targets were observed with GIRAFFE in the field of γ Vel, while in Cha I GIRAFFE spectra of 674 stars were secured. Far fewer spectra were acquired with UVES (80 targets in γ Vel and 48 in Cha I). A detailed description of the target selection and spectroscopic observations is given by Jeffries et al. (2014) for γ Vel and Spina et al. (2014b) for Cha I.

Sacco et al. (2014) describe the reduction procedure for the UVES spectra, while for the GIRAFFE ones we refer the reader to Jeffries et al. (2014) and Lewis et al. (2014, in prep.).

The spectra observed in the γ Vel and Cha I fields, which are publicly available[3], have been analyzed by the GES working groups WG8 and WG12. WG8 derives radial velocity (RV) and projected rotational velocity ($v \sin i$) both for GIRAFFE (Jeffries et al. 2014) and UVES spectra (Sacco et al. 2014). WG12 is the working group responsible for the analysis of PMS clusters and delivers spectral type (SpT), effective temperature ($T_{\rm eff}$), surface gravity ($\log g$), $v \sin i$ (derived with a different approach than WG8), iron abundance ([Fe/H]), microturbulence (ξ), veiling (r), lithium equivalent width at λ6707.8 Å ($EW_{\rm Li}$), lithium abundance ($\log n_{\rm Li}$), Hα/Hβ equivalent widths ($EW_{\rm H\alpha}/EW_{\rm H\beta}$) and fluxes ($F_{\rm H\alpha}/F_{\rm H\beta}$), H$\alpha$ full-width at 10% of peak height (10%$W_{\rm H\alpha}$), mass accretion rate ($\dot{M}_{\rm acc}$), and other elemental abundances ([X/H]).

2.1. Member selection

For the γ Vel cluster, WG8 produced reliable values of RV and $v \sin i$ for most of the 1242 targets observed with GIRAFFE. The analysis performed by WG12, restricted to spectra with S/N ≥ 20, provided values of the main stellar parameters (SpT, $T_{\rm eff}$, $\log g$) for 1078 stars. Among the 80 stars observed with UVES, the stellar parameters were determined for 68 stars, the remaining being spectroscopic binaries (six stars) or early-type and rapidly-rotating stars.

For the 674 stars observed with GIRAFFE in the Cha I field, WG12 released values of the main stellar parameters for 556 of them, while 42 out of the 48 UVES sources have atmospheric parameter entries in the GESviDR1Final catalogue. As for γ Vel, the fundamental parameters were not derived for the double-lined spectroscopic binaries (SB2s), the early-type and rapidly-rotating stars and all the sources that have a spectrum with S/N< 20.

In the following, we use the membership criteria adopted by Jeffries et al. (2014) and Spina et al. (2014b) for γ Vel and Cha I, respectively. The selection performed by these authors was based on the strength of the lithium line at λ6707.8 Å (a reliable indicator of membership to young clusters), the surface gravity (to identify and discard lithium-rich giant contaminants in the field), and the position in the color-magnitude diagram (CMD, to recognize the cluster sequence). We refer to the objects preselected with these criteria as "lithium members". The final members are those which fulfill an additional criterion based on their radial velocity: $8 \leq RV \leq 26\,{\rm km\,s^{-1}}$ and $10 \leq RV \leq 21\,{\rm km\,s^{-1}}$ for γ Vel and Cha I, respectively (see Fig. 1). The reader is referred to the aforementioned papers for a wide description of the membership analysis and the selection criteria. The only difference with respect to the aforementioned works is that we have slightly fewer targets, because we have restricted the analysis for deriving stellar parameters and chromospheric emission only to the spectra with a S/N larger than 20 per spectral point. The RV distribution of the lithium members and targeted non-members of γ Vel and Cha I clusters, according to the above criteria is displayed in Fig. 1. The finally selected members are represented by the hatched areas in the histograms of Fig. 1.

The parameters for the members of γ Vel and Cha I clusters are reported in Tables 2 and 3, respectively.

In the end, our study is based on 132 members of γ Vel cluster observed only with GIRAFFE (154 lithium members) and on eight lithium members observed with UVES (six of them are also RV members and two are also observed with GIRAFFE). For Cha I, our analysis is based on 59 GIRAFFE and 15 UVES members. We remark that the SB2s, identified by means of the cross-correlation functions, are not included in our study. However, the SB2s in our sample are rather few (28 in γ Vel and 6 in Cha I) in comparison to the total number of targets (both members and non-members) and most of them cannot be considered as candidate members on the base of lithium. Thus, we do not expect that their exclusion can have appreciably biased our sample. The same occurs for the rejection of the low S/N spectra. Compared to the 208 lithium members of γ Vel reported by Jeffries et al. (2014), we have 54 stars less, i.e. our sample is roughly 3/4 of that one. We are missing mostly some of the coolest stars, but this cut should have not biased the sample with respect to rotation velocity, Hα flux, and accretion.

3. Analysis

3.1. Projected rotation velocity and veiling

In the GES analysis of PMS clusters, SpT, $v \sin i$, and veiling are produced by one analysis node of WG12 that makes use of ROTFIT, an IDL[4] code developed for deriving SpT, $T_{\rm eff}$, $\log g$, [Fe/H], r, and $v \sin i$ of the targets. This code compares the target spectrum with a grid of templates composed of high-resolution ($R \simeq 42\,000$) spectra of 294 slowly-rotating, low-activity stars retrieved from the ELODIE Archive (Moultaka et al. 2004). The templates were brought to the GIRAFFE resolution, aligned in wavelength with the target spectrum by means of the cross-correlation, resampled on its spectral points and artificially broadened by convolution with a rotational profile of increasing $v \sin i$ until the minimum of χ^2 is reached (see Frasca et al. 2003, 2006). The list of templates along with their spectral type and atmospheric parameters is reported in Table 4.

To verify the ability of the procedure to derive the $v \sin i$ and to check the minimum detectable value with GIRAFFE spectra, we ran Monte Carlo simulations with two slowly-rotating stars, namely 18 Sco (G2 V) and δ Eri (K0 IV). The

[3] http://www.eso.org/sci/observing/phase3/data_releases.html

[4] IDL (Interactive Data Language) is a registered trademark of Exelis Visual Information Solutions.

Table 1. Summary of the GES observations of γ Vel and Cha I.

Instrument	Range (Å)	Resolution ($\lambda/\Delta\lambda$)	γ Vel # stars	γ Vel # members	Cha I # stars	Cha I # members
UVES	4764–6820	47 000	80	8	48	15
GIRAFFE	6445–6815	17 000	1242	132	647	59

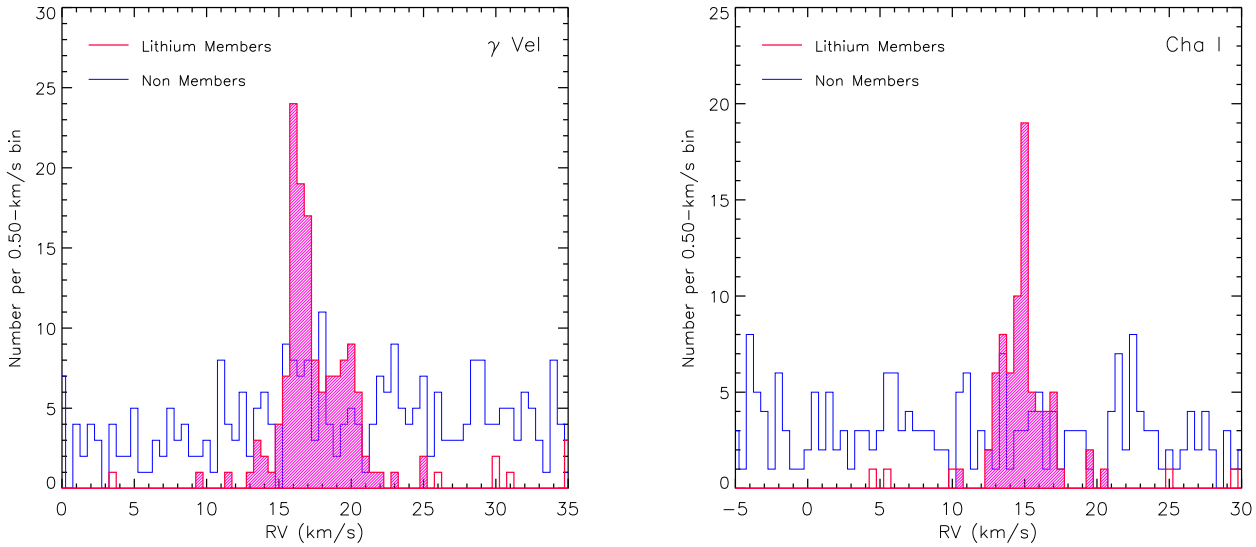

Fig. 1. Radial velocity distribution of γ Vel (*left panel*) and Cha I (*right panel*) stars. Thick (red) and thin (blue) lines represent the histograms of "lithium members" and targeted non-members, respectively. Lithium members fulfilling also the *RV* criterion are represented by the red hatched area. Note in γ Vel the double peak in the *RV* distribution of members and the total absence of such peaks in that of non-members.

GIRAFFE spectra of these stars were artificially broadened by convolution with a rotation profile of increasing $v \sin i$ (in steps of 2 km s^{-1}) and a random noise corresponding to a signal-to-noise ratio S/N=20 and S/N=100 was added. We made 100 simulations per each $v \sin i$ and S/N running ROTFIT on every simulated spectrum. After the first nearly flat part where the $v \sin i$ is unresolved, the linear trend between measured and "theoretical" $v \sin i$ starts at 6–8 km s^{-1} (Fig. 2). We thus consider all the $v \sin i$ values lower than 7 km s^{-1} as upper limits.

As mentioned above, the $v \sin i$ for the GIRAFFE spectra is also measured, with a different procedure by WG8 along with the *RV* determination and the data are stored in the VELCLASS fits extension of the reduced spectra. The results of both procedures are compared for the stars in the γ Vel field in Fig. 3. The overall agreement between the two sets of values is apparent. However, in this study we use the $v \sin i$ values released by WG12.

The code ROTFIT is also able to evaluate the veiling of the spectra. Since this greatly increases the computing time, we have left r free to vary in the code only when a veiling can be expected, i.e. for objects with a likely accretion. In the WG12, the "accretor candidates" are selected as those stars with $10\%W_{\rm H\alpha} \geq 270$ km s^{-1} (White & Basri 2003). However, for these two young clusters, we preferred to use less restrictive criteria to check whether a significant veiling can be found by the code also for objects just under the above cutoff. Thus, we ran the code with the veiling option enabled for all objects with $10\%W_{\rm H\alpha} \geq 200$ km s^{-1}. We found a handful of objects with $200 < 10\%W_{\rm H\alpha} < 270$ km s^{-1} and a non-zero veiling, all of which with $r < 0.25$, i.e. likely not significant. The uncertainty of veiling determinations is in the range 20–50 % whenever $r > 0.25$ (see Tables 2 and 3).

When searching for the best templates that reproduce the veiled stars, we considered the following equation:

$$\left(\frac{F_\lambda}{F_C}\right)_r = \frac{\frac{F_\lambda}{F_C} + r}{1 + r}\,, \qquad (1)$$

where F_λ and F_C represent the line and continuum fluxes, respectively. Moreover, r was let free to vary to find the minimum χ^2, assuming it constant over a limited wavelength range (which is 100 Å for the 18 UVES spectral segments independently analyzed and about 300 Å for the GIRAFFE spectra). In Fig. 4 we show an example of an accreting star in Cha I with $r = 0.4$, as found by ROTFIT.

We want to point out that the veiling is better and safer determined from the UVES spectra than from the GIRAFFE ones because the former have a much wider spec-

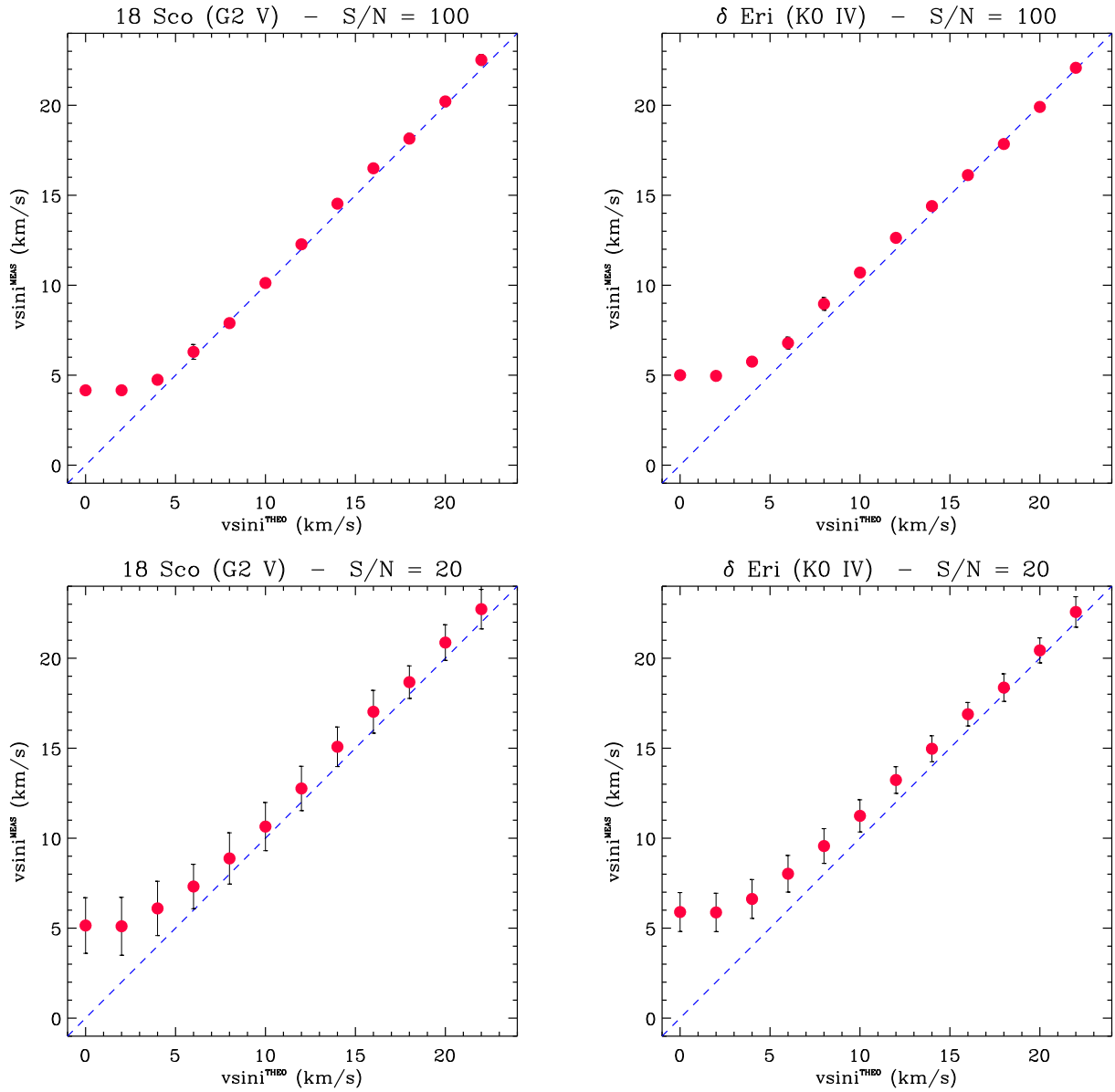

Fig. 2. Results of the Monte Carlo simulations on $v \sin i$ made with GIRAFFE spectra of two slowly-rotating stars for S/N=100 (*upper panels*) and S/N=20 (*lower panels*). The average $v \sin i$ measured with our procedure (dots) are plotted against the "theoretical" $v \sin i$ to which the spectra have been broadened. The one-to-one relation is plotted with a dotted line.

tral coverage and include several strong lines suitable for the measurement of this parameter. This is testified by the internal agreement between values of veiling derived from adjacent segments (see also Biazzo et al. 2014). In the case of HR15N GIRAFFE spectra, we can obtain only a rather rough estimate of veiling.

3.2. Spectral Energy Distribution

To obtain the stellar bolometric luminosities of all analyzed members of γ Vel and Cha I, we constructed the spectral energy distribution (SED) of the targets using the optical and near-infrared (NIR) photometric data available in the literature.

For the γ Vel stars, we combined optical BVI_C (Jeffries et al. 2009) and 2MASS JHK_s (Skrutskie et al. 2006) photometry. Moreover, *Spitzer* mid-infrared (MIR) data from Hernández et al. (2008) were also available for about 79 % of the sources. For the objects in Cha I, we used BVR photometry from the NOMAD catalog (Zacharias et al. 2004) and Cousins I_C magnitudes from the DENIS database that were combined with 2MASS JHK_s and *Spitzer* data (Luhman et al. 2008).

We then adopted the grid of NextGen low-resolution synthetic spectra, with $\log g$ in the range 3.5–5.0 and solar metallicity by Hauschildt et al. (1999), to fit the optical-NIR portion (from B to J band) of the SEDs, similarly to what done by Frasca et al. (2009) for stars in the Orion Nebula Cluster.

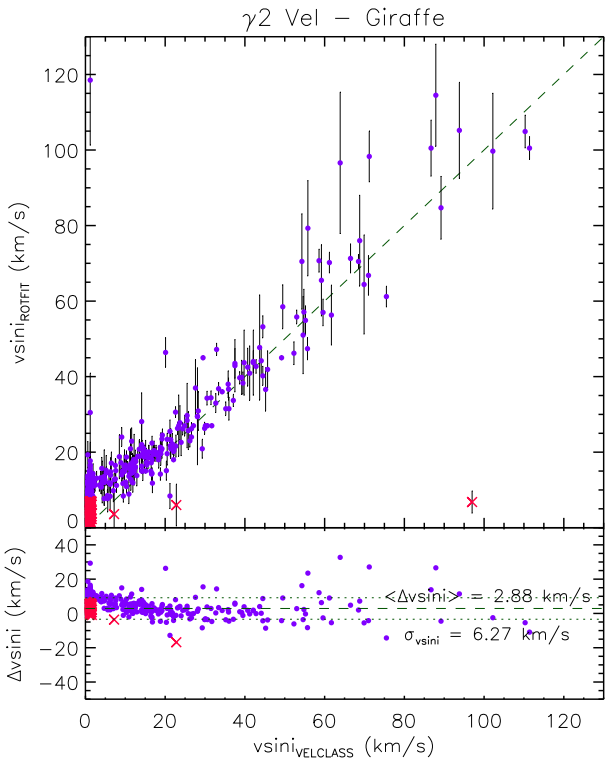

Fig. 3. Comparison between the $v \sin i$ measured by the VELCLASS (WG8) and ROTFIT (WG12) procedures for the stars in the γ Vel field. The ROTFIT's $v \sin i$ values lower than 7 km s^{-1} are denoted by red crosses.

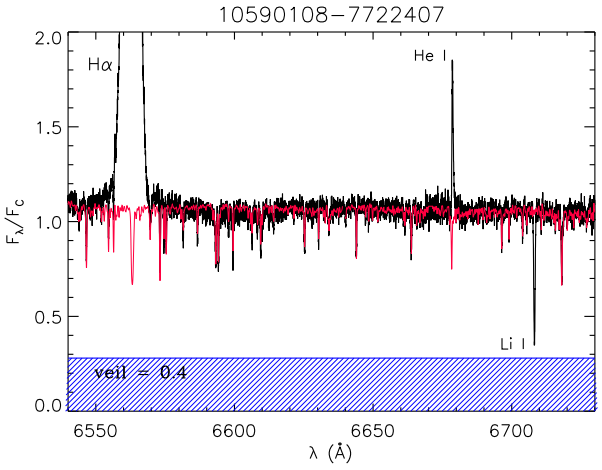

Fig. 4. UVES spectrum of an accreting star in Cha I (thick black line) with overplotted the rotationally-broadened and veiled best template (thin red line). A wavelength independent veiling of 0.4 (hatched area) was found by ROTFIT.

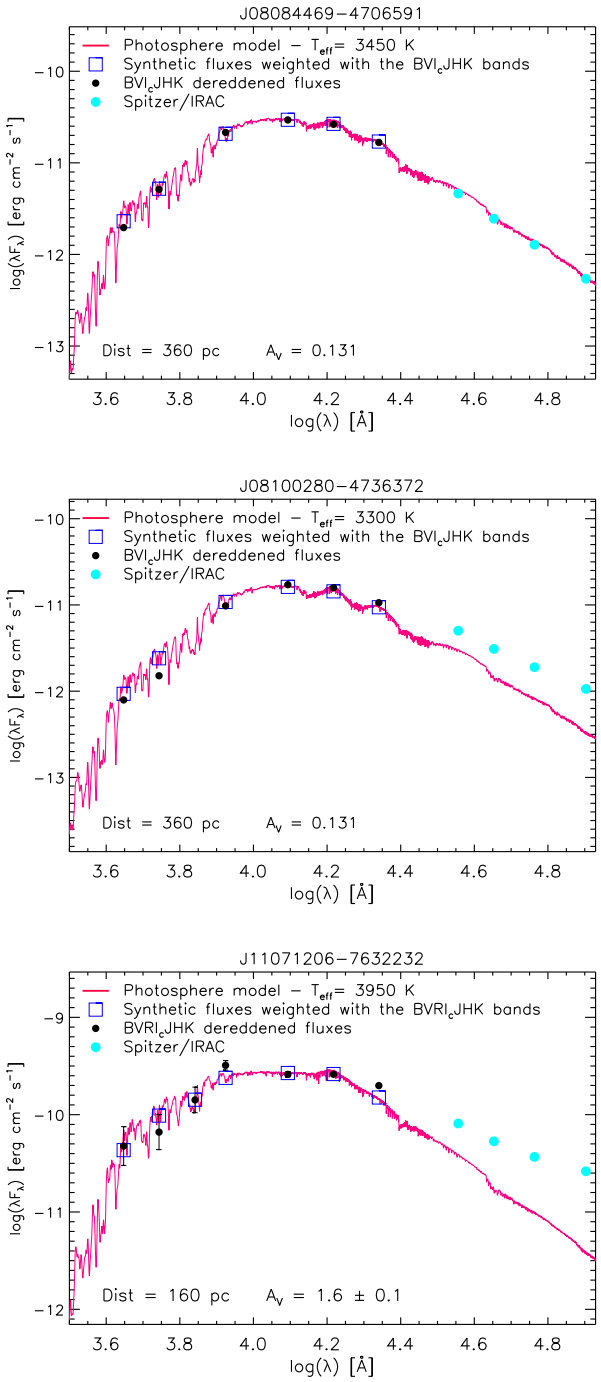

Fig. 5. Spectral energy distributions (dots) of two members of γVel cluster (*upper and middle panels*) and one member of the young Cha I association (*lower panel*). In each panel, the best fitting low-resolution NextGen spectrum (Hauschildt et al. 1999) is displayed by a continuous line. The SEDs of the two accretors (*middle and lower panels*) display a MIR excess, typical of Class II sources.

For the stars in the γ Vel cluster, we adopted the distance of 360 pc and the extinction $A_V = 0.131$ mag found by Jeffries et al. (2009) and fixed the effective temperatures of the targets to the values found by the spectral analysis of WG12 and delivered in the first internal data release (iDR1). We let the stellar radius ($R_\star$) vary until a minimum χ^2 was reached. The stellar luminosity was then obtained by integrating the best-fit model spectrum. We found a poor SED fitting only for three members of the cluster, namely J08101877−4714065, J08114456−4657516, and J08110328−4716357. This was likely due to a bad $T_{\rm eff}$ determination. For these stars we have used instead the

photometric temperatures that are derived as described in Lanzafame et al. (2014). For the members of Cha I, which are scattered in a wide sky region with dense molecular clouds, we made the fit of the SEDs with the extinction parameter free to vary. The SEDs of two members of γ Vel, with and without MIR excess, and one of Cha I are shown, as an example, in Fig. 5.

To our knowledge, no spectroscopic determination of effective temperaure from spectroscopy is available in the literature for the members of γ Vel, while, for several objects in Cha I, Luhman (2007) reported SpT, along with the corresponding $T_{\rm eff}$ values, derived from low-resolution spectroscopy. The comparison between our $T_{\rm eff}$ values and Luhman's ones shows a good agreement in the low temperature domain ($T_{\rm eff}$ <3800–4000 K), while a systematic difference appears for warmer stars in the sense that Luhman's values are lower than our ones by 200–400 K (up to 800 K in the worst case). We think that the different spectral range and the lower resolution of Luhman's spectra can be responsible for such a discrepancy. Moreover, some scatter could be also introduced by the binarity of a few sources (e.g., Nguyen et al. 2012; Daemgen et al. 2013). The bolometric luminosities, compared to the values reported by Luhman (2007), do not show any relevant offset ($\approx -13\%$), but the rms deviation is rather large ($\approx 66\%$).

3.3. HR diagram

In Figure 6, we report the position of our targets in the HR diagram, along with the PMS evolutionary tracks and isochrones calculated by Baraffe et al. (1998). The effective temperatures are those from the WG12 analysis delivered in the iDR1, while the stellar luminosities are derived from the SED analysis illustrated in Sect. 3.2. Most of the γ Vel stars are located between the isochrones at 4 and 30 Myr, while the Cha I members lie higher in the diagram, as expected according to their younger age.

We used the HR diagram and the evolutionary tracks for estimating the masses of the targets by minimizing the quantity:

$$\chi^2 = \frac{(T_{\rm eff} - T_{\rm mod})^2}{\sigma^2_{T_{\rm eff}}} + \frac{(L - L_{\rm mod})^2}{\sigma^2_L}\,, \qquad (2)$$

where $T_{\rm eff}$ and $\sigma_{T_{\rm eff}}$ are the stellar effective temperature and its error, respectively, and $T_{\rm mod}$ is the temperature of the nearest evolutionary track. Analogously, L and σ_L are the stellar bolometric luminosity and its error, respectively, while $L_{\rm mod}$ is the luminosity of the nearest track.

The masses, which are also reported in Tables 2 and 3, are used in Sect. 3.5 to evaluate the mass accretion rate.

3.4. Equivalent width and flux of the Hα and Hβ lines

The most useful indicator of chromospheric activity in the HR15N GIRAFFE setup is the Hα line, while the UVES spectra include also, among other diagnostics, the Hβ line. Unlike the chromospheric and transition region lines at ultraviolet wavelengths, the contribution of the photospheric flux in these optical lines is very important and must be removed to isolate the pure chromospheric emission that often is only filling-in the line cores. Thus, for the WG12 analysis, we have calculated EWs and fluxes by using the spectral subtraction method (see, e.g., Frasca & Catalano 1994; Montes et al. 1995, and references therein) to remove the photospheric flux and emphasize the chromospheric emission in the line core (see Fig. 7). Thanks to this procedure, the net equivalent width of the Hα and Hβ lines ($EW_{\rm H\alpha}$, $EW_{\rm H\beta}$) were derived (see Tables 2, 3, and 5). In the example shown in Fig. 7, the Hα line is totally filled-in by emission and its core is just reaching the continuum level, while the Hβ emission filling-in the line core is only detected after the subtraction of the low-activity template. In both the Hα and Hβ regions, the photospheric absorption lines are mostly removed by the subtraction.

Whenever a veiling $r > 0$ was found, it has been introduced in the low-activity template before the subtraction, following Eq. (1), so as to reproduce the photospheric lines of the target. However, the EWs reported in Table 2 and 3 and stored in the GESviDR1Final catalogue are not corrected for veiling. To obtain the corrected values, they must be multiplied by $(1 + r)$.

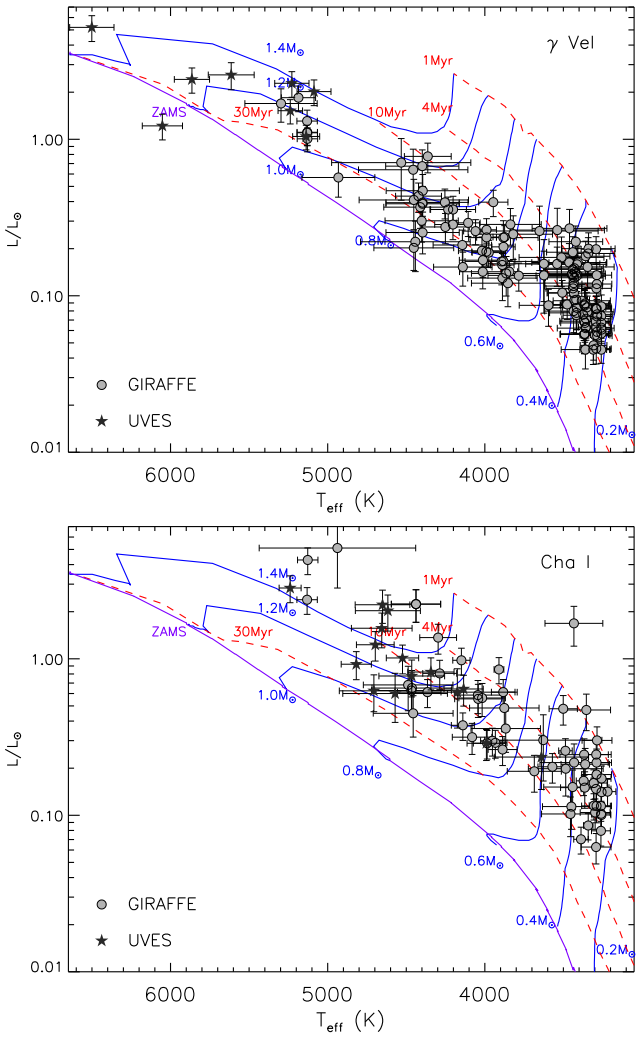

Fig. 6. HR diagram of γ Vel (*upper panel*) and Cha I (*lower panel*) members for both UVES and GIRAFFE data. The evolutionary tracks of Baraffe et al. (1998) are shown by solid lines with the labels representing their masses. Similarly, the isochrones (from 1 to 30 Myr) by the same authors are shown with dashed lines. The ZAMS position is also represented by a solid line.

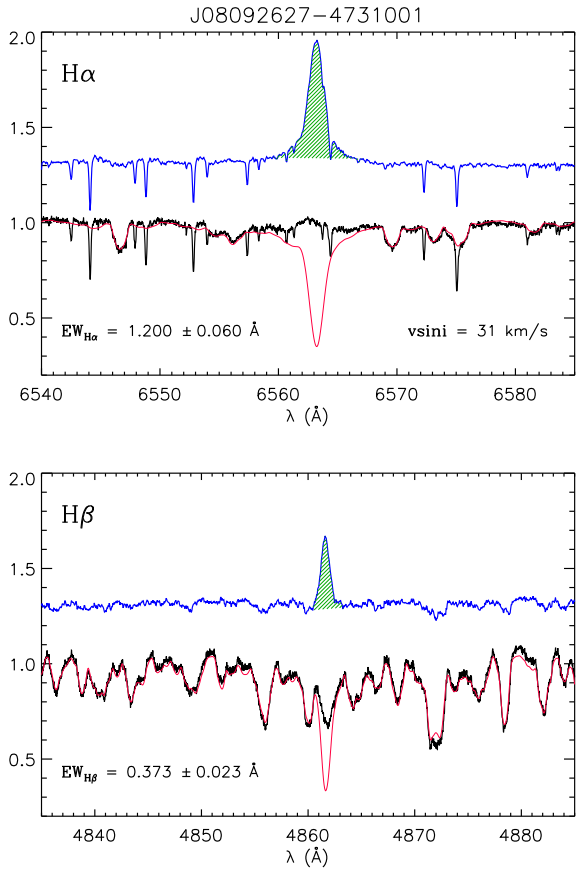

Fig. 7. Example of the spectral subtraction method with UVES spectra in the Hα (*upper panel*) and Hβ (*lower panel*) regions for an active star in γ Vel. The target spectrum is represented by a black solid line, while the best fitting reference spectrum of a low-activity star artificially broadened at the $v \sin i$ of the target is overplotted with a thin red line. In both panels, the difference spectrum (blue line) is displayed shifted upwards by 1.3 for clarity. The residual Hα and Hβ profiles integrated over wavelength (hatched green areas) provide the net equivalent widths ($EW_{\rm H\alpha}$ and $EW_{\rm H\beta}$). The narrow absorption features visible in the upper panel are telluric water vapor lines.

$EW_{\rm H\alpha}$ is plotted as a function of $T_{\rm eff}$ for members of γ Vel and Cha I in Fig. 8. The largest $EW_{\rm H\alpha}$ are observed for cooler stars, due to contrast effects (i.e. the Hα emission stands out against a low continuum level). This behaviour is commonly observed in young clusters and associations (see, e.g. Stauffer et al. 1997; Kraus et al. 2014).

A better diagnostic of chromospheric activity is the line surface flux (indicator of radiative losses) that can be derived from the net line equivalent width as

$$F_{\rm H\alpha} = F_{6563} EW_{\rm H\alpha} \quad (3)$$
$$F_{\rm H\beta} = F_{4861} EW_{\rm H\beta}\,, \quad (4)$$

where F_{6563} and F_{4861} are the continuum surface fluxes at the Hα and Hβ wavelengths, respectively, and are evaluated from the NextGen synthetic low-resolution spectra (Hauschildt et al. 1999) at the stellar temperature and surface gravity provided by the GES consortium.

As a further activity index, we have also calculated the ratio of the chromospheric emission in the Hα line to the total bolometric emission:

$$R'_{\rm H\alpha} = L_{\rm H\alpha}/L_{\rm bol} = F_{\rm H\alpha}/(\sigma T_{\rm eff}^4). \quad (5)$$

The behavior of the activity indicators as a function of stellar parameters is described in Sects. 4.2 and 4.3.

3.5. Mass accretion rate diagnostics

We considered as mass accretion rate ($\dot{M}_{\rm acc}$) for the members of both clusters the values reported by the GES consortium in the iDR1 (see Lanzafame et al. 2014), which are based on the measurements of the $10\%W_{\rm H\alpha}$ performed on the observed Hα profiles, without subtracting the low-activity template. The values of $\dot{M}_{\rm acc}$ were computed using the Natta et al. (2004) relationship:

$$\log \dot{M}_{\rm acc}^{10\%W} = -12.89(\pm0.3) + 9.7(\pm0.7)10^{-3} 10\%W_{\rm H\alpha}, \quad (6)$$

with $10\%W_{\rm H\alpha}$ in km s^{-1} and $\dot{M}_{\rm acc}$ in $M_\odot$ yr^{-1}. Typical errors in $\log \dot{M}_{\rm acc}$ from this relation are about $0.4 - 0.5$ dex. Natta et al. (2004) provided this relation for objects with $10\%W_{\rm H\alpha} > 200$ km s^{-1}, corresponding to $\log \dot{M}_{\rm acc} \sim -11$. For this reason, the GES data contains $\dot{M}_{\rm acc}$ for stars with $10\%W_{\rm H\alpha}$ >200 km s^{-1}, but only the objects that meet the most restricted criterion, $10\%W_{\rm H\alpha} > 270$ km s^{-1} (White & Basri 2003), are considered as accretor candidates.

An independent way of deriving the mass accretion rate is based on the total energy flux in emission lines. We used the empirical relations between accretion luminosity ($L_{\rm acc}$) and the luminosity in the Hα line ($L_{\rm H\alpha}$), which were recently derived by Alcalá et al. (2014) from X-Shooter@VLT data to estimate $L_{\rm acc}$. The line luminosity was calculated as $L_{\rm H\alpha} = 4\pi R_\star^2 F_{\rm H\alpha}$, where the stellar radius ($R_\star$) was derived from the analysis of the SEDs (Sect. 3.2), while the surface flux ($F_{\rm H\alpha}$) was obtained using the net EW of the Hα line, as described in Sect. 3.4. Unlike several previous works, we have decided to use the net Hα EW, where we have removed the contribution of the photospheric line absorption, to have a single diagnostic for both the chromospheric emission and accretion, which are simultaneously investigated. This choice allows us to treat properly the stars with a faint emission or only a filled-in line core. However, for the spectra showing the line as a pure emission feature above the continuum, we have also measured the EW of the Hα line without subtracting the low-activity template. We found a negligible flux difference (within 0.1 dex), between EWs from subtracted and unsubtracted spectra, for all the accreting objects, suggesting that the flux calculated with the net EWs can be safely used in comparison with previous works.

The mass accretion rate ($\dot{M}_{\rm acc}$) was then derived from $L_{\rm acc}$ using the relationship by Hartmann (1998):

$$\dot{M}_{\rm acc}^{EW} = \left(1 - \frac{R_\star}{R_{\rm in}}\right)^{-1} \frac{L_{\rm acc} R_\star}{G M_\star}, \quad (7)$$

where the stellar mass $M_\star$ for each star was estimated from the theoretical evolutionary tracks, as described in Sect. 3.3, and the inner-disk radius $R_{\rm in}$ was assumed to be $R_{\rm in} = 5R_\star$ (Hartmann 1998). Contributions to the error budget on $\dot{M}_{\rm acc}$ include uncertainties on stellar mass,

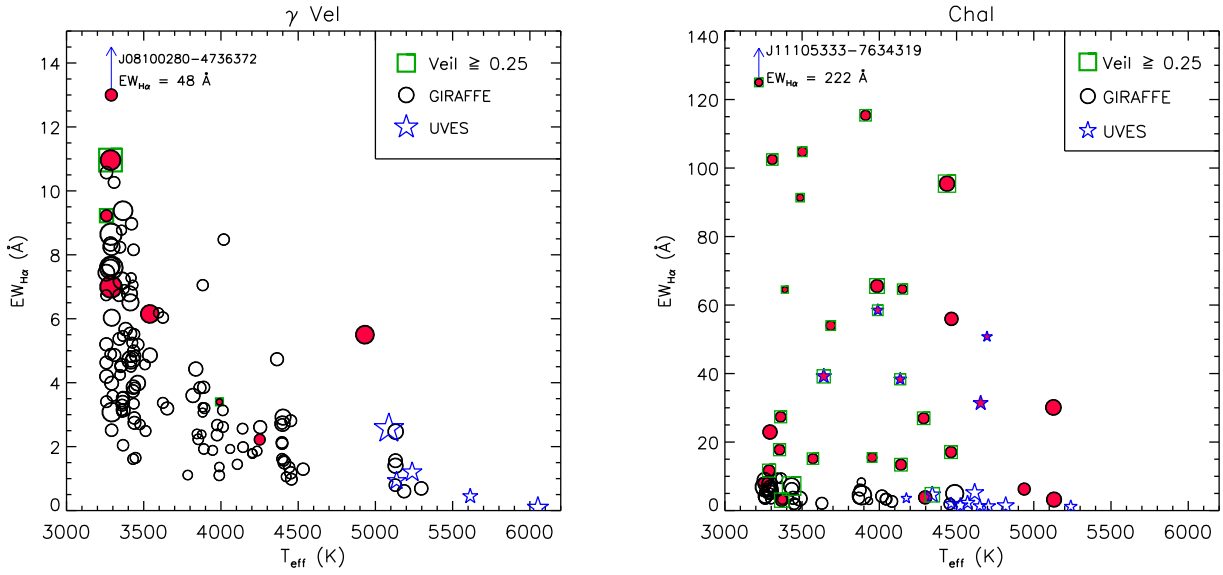

Fig. 8. Net Hα equivalent width versus $T_{\rm eff}$ of the γ Vel (*left panel*) and Cha I (*right panel*) members observed with GIRAFFE and UVES. The symbol size scales with the $v \sin i$. Filled symbols denote the accretor candidates ($10\%W_{\rm H\alpha} > 270$ km s^{-1}), while the targets with a significant amount of veiling ($r \geq 0.25$) are enclosed into open squares. The two arrows represent the targets with $EW_{\rm H\alpha}$ out of the range.

stellar radius, inner-disk radius, and $L_{\rm acc}$. Assuming mean errors of $\sim 0.15\,M_{\odot}$ in $M_{\star}$ and $\sim 0.1\,R_{\odot}$ in $R_{\star}$, 5–10% as relative error in $EW_{\rm H\alpha}$, 10% in the continuum surface flux at the Hα line used for deriving $F_{\rm H\alpha}$, and the uncertainties in the relationships by Alcalá et al. (2014), we estimate a typical error in $\log \dot{M}_{\rm acc}$ of ~ 0.5 dex.

The use of the Hα EW allows us to define as "confirmed accretors" those objects which fulfill the requirements proposed by White & Basri (2003, see their Fig. 7) and based on both Hα EW and *SpT*. Adopting these criteria, we identified 26 and 3 accretors in Cha I and γ Vel, respectively. Similar results are found adopting the selection criteria proposed by Barrado y Navascués & Martín (2003, see their Fig. 5). We remark that 24 out of 26 accretors in Cha I were classified as flat or Class II IR sources by Manoj et al. (2001) and Luhman et al. (2008). For the two remaining objects no IR classification is available in the literature. We classified 5 Cha I and 3 γ Vel members, which are close to the border line proposed by White & Basri (2003) or Barrado y Navascués & Martín (2003), as "possible accretors". All but one of the five possible accretors in Cha I are Class II objects, while the source J11071915−7603048 is a Class III star (Luhman et al. 2008) with $10\%W_{\rm H\alpha} \sim 370$ km s^{-1}, $v \sin i \sim 10$ km s^{-1} and $EW_{\rm H\alpha} = 15.2$ Å (see Table 3). Two out of our eight confirmed/possible accretors in γ Vel are reported as Class II objects by Hernández et al. (2008), while all the remaining six sources are all classified as Class III.

In Fig. 9, the comparison of the two accretion rate estimates is shown. The difference between the two determinations of $\dot{M}_{\rm acc}$ for a given object is quite large (~ 0.8 dex for Cha I and ~ 0.7 dex for γ Vel, on average). Similar results were also found by Costigan et al. (2012) who studied the variability of mass accretion in a sample of 10 stars in Cha I. The same authors suggest that the $10\%W_{\rm H\alpha}$ does not give reliable estimates of average accretion rates, especially when single-epoch observations were performed. The inconsistencies we found between the two $\dot{M}_{\rm acc}$ determinations may also be due to the effects of Hα extra-absorption by stellar winds on the emission line profile produced by the accretion flow, and to line emission not due to accretion, which can affect the 10% width and the Hα EW in a very different way. For instance, an extra absorption wing that produces a strongly asymmetric or a P-Cygni profile could cause an underestimate of the 10% width much larger than for the Hα EW. A Spearman's rank correlation analysis (Press et al. 1992) applied to the Cha I data provides a coefficient $\rho = 0.10$ with a significance of its deviation from zero $\sigma = 0.61$ which testifies the large data scatter.

For our Cha I data, most of the spread is due to seven stars showing differences in the accretion rates larger than 1 dex. In particular, for the three stars with $(\log \dot{M}_{\rm acc}^{10\%W} - \log \dot{M}_{\rm acc}^{EW}) > +1.0$ dex, namely J11092379−7623207, J11071206−7632232, and J11075809−7742413 (with $v \sin i$ of some km s^{-1}), the difference is most probably due to the presence of wide wings and/or strong central reversals in their spectra at the epoch of our observations. This overestimates the $10\%W_{\rm H\alpha}$ and, therefore, the mass accretion rate derived from this diagnostic. For the four stars with $(\log \dot{M}_{\rm acc}^{10\%W} - \log \dot{M}_{\rm acc}^{EW}) < -1.0$ dex, the difference between the two $\dot{M}_{\rm acc}$ values could be due instead to the Natta et al. (2004) relation in this range of values. In fact, as pointed out by Alcalá et al. (2014), for objects with $10\%W_{\rm H\alpha} < 400$ km s^{-1}, the Natta et al. (2004) relation tends to underestimate $\dot{M}_{\rm acc}$ by ~ 0.6 dex with respect to the determinations coming from primary diagnostics such as the continuum-excess modelling; however, the differences may be up to about one order of magnitude. Indeed, the stars in our sample with $(\log \dot{M}_{\rm acc}^{10\%W} - \log \dot{M}_{\rm acc}^{EW}) < -1.0$ dex have $270 < 10\%W_{\rm H\alpha} \lesssim 440$ km s^{-1}. Herczeg & Hillenbrand (2008), Fang et al. (2009),

and Costigan et al. (2012) reported similar findings in Taurus, L1641, and Cha I, respectively.

Concerning the data that we acquired for γ Vel, only the possible accretor J08105600−4740069 shows ($\log \dot{M}_{\rm acc}^{10\%W} - \log \dot{M}_{\rm acc}^{EW}$) > 1 dex. This source displays wide Hα wings, $10\%W_{\rm H\alpha}$ close to 400 km s^{-1}, and a moderate rotation rate ($v \sin i \sim 15$ km s^{-1}). It is also a Class II object according to Hernández et al. (2008).

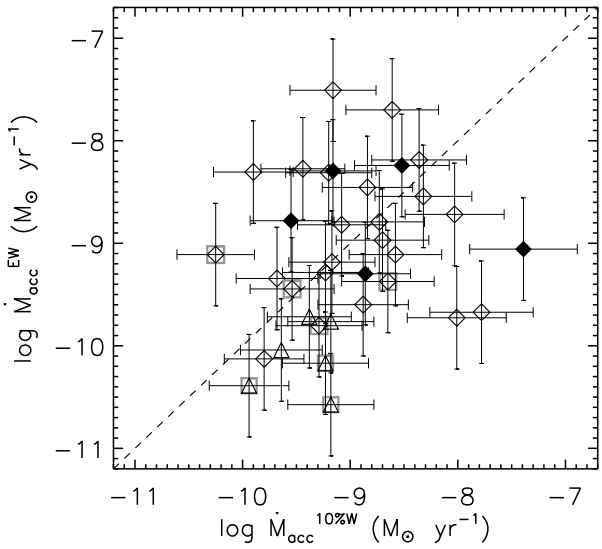

Fig. 9. Accretion rates from $EW_{\rm H\alpha}$ versus accretion rates from $10\%W_{\rm H\alpha}$ for Cha I (diamonds) and γ Vel (triangles) stars. Empty and filled symbols refer to GIRAFFE and UVES data, respectively. Squares show the possible accretors. The dashed line is the one-to-one relation.

4. Results and Discussion

4.1. Projected rotation velocity

The availability of a large dataset of cluster members with measured projected rotational velocity allows us to investigate the distribution of stellar rotation rates and their dependence on fundamental stellar parameters.

Figure 10 shows the distribution of $v \sin i$ for both clusters. The $v \sin i$ was measured for all 132 GIRAFFE members of the γ Vel cluster according to the three criteria adopted by Jeffries et al. (2014), namely CMD, lithium line, and RV. We also have $v \sin i$ determinations for the eight late-type members of γ Vel observed with UVES. Two of them have a RV not compatible with the cluster, but they fulfill all the other criteria and are considered as members by Spina et al. (2014a). Two of these eight UVES targets have been also observed with GIRAFFE in different observing blocks, but in this study we considered for them the UVES data. The $v \sin i$ distribution (left panel in Fig. 10) displays a main peak at about 10 km s^{-1} with a tail toward faster rotators. Despite the blurring of the distribution produced by the inclination angles, compared to a rotation period distribution, its appearance is consistent with a mixture of stars that have spun up and others that have maintained a slow rotation rate likely due to efficient disk locking. We constructed the $v \sin i$ distributions for the stars that can be unambiguously associated with each of the two kinematical populations identified by Jeffries et al. (2014) and clearly revealed by the double-peaked distribution of the radial velocities (see Fig. 1). The population A, centered at about 16.7 km s^{-1} with an intrinsic dispersion $\sigma_{\rm A} = 0.34$ km s^{-1} is found to be older by about 1–2 Myr than the component B, which is centered at 18.8 km s^{-1} and shows a wider dispersion ($\sigma_{\rm B} = 1.60$ km s^{-1}). As already noted by the same authors, the stars in the population B tend to rotate faster, on average, than those of the population A. A two-sided Kolmogorov-Smirnov (KS; Press et al. 1992) test of the cumulative $v \sin i$ distributions of the two populations reveals a significant difference, the significance level resulting to be $P_{\rm KS} = 0.03$. This behaviour cannot be attributed to the age difference between the two groups, which is too small in comparison with the typical times of rotation evolution and is more likely related to different environmental conditions during their early life. The massive binary system γ^2 Vel seems to be slightly younger than the low-mass stars of the population A (Jeffries et al. 2014). Thus, these stars may not have been affected by the strong radiation field and stellar wind from γ^2 Vel during the first few Myr of their life, while the population B might have experienced such an effect. As a result, the disks around the members of population B could have been dispersed earlier than those of the population A, with a shorter disk-locking effect and a faster spin up.

For Cha I, the distribution displays a peak around 10 km s^{-1}, which is narrower than that of γ Vel, and a non negligible fraction of relatively fast rotators (up to ∼40 km s^{-1}). A KS test of the γ Vel and Cha I $v \sin i$ distributions shows only a marginal difference ($P_{\rm KS} = 0.36$). This is in agreement with the results of studies of the evoultion of stellar rotation (e.g., Messina et al. 2010; Spada et al. 2011) that show only a moderate increase of the average rotation rate between the ages of these two clusters.

4.2. Hα flux

In Fig. 11 we show the Hα surface flux as a function of the effective temperature. This figure clearly shows that the nearly exponential behavior displayed by $EW_{\rm H\alpha}$ as a function of $T_{\rm eff}$ (Fig. 8) disappears when the flux is used. In this figure we do not use squares to enclose the stars with a veiling $r \geq 0.25$, as we did in Fig. 8, but we display with arrows the flux values obtained by correcting the EWs for the dilution caused by the veiling, i.e. multiplying by the factor $(1 + r)$.

We have drawn, in both panels of Fig. 11 a dashed straight line that demarcates the domain of accretors from that of chromospherically active stars. This "dividing line", which is empirically defined by the upper boundary of the chromospheric fluxes (empty symbols) of stars in both clusters, is expressed by:

$$\log F_{\rm H\alpha} = 6.35 + 0.00049(T_{\rm eff} - 3000)\,. \quad (8)$$

For comparison, we have also overplotted in Fig. 11 the "saturation limit" adopted by Barrado y Navascués & Martín (2003) to separate classical from weak T Tauri stars, where we adopted the SpT–$T_{\rm eff}$ calibration of Pecaut & Mamajek (2013). The

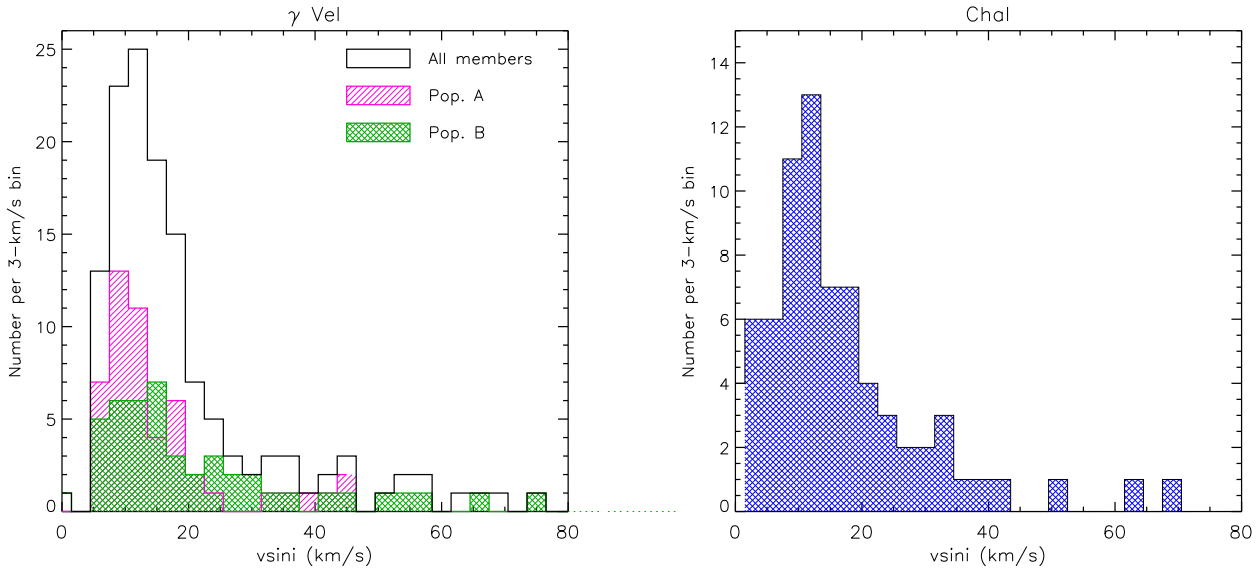

Fig. 10. *Left panel:* The distribution of $v \sin i$ for the members of γ Vel (empty histogram) showing a main peak centered at about 10 km s^{-1} with a tail towards faster rotators. The two kinematic subsamples A and B identified by Jeffries et al. (2014) display slightly different distributions (hatched and filled histograms), with higher frequency of faster rotators for the population B. *Right panel:* The distribution of $v \sin i$ for the members of Cha I, peaked at about 10 km s^{-1}.

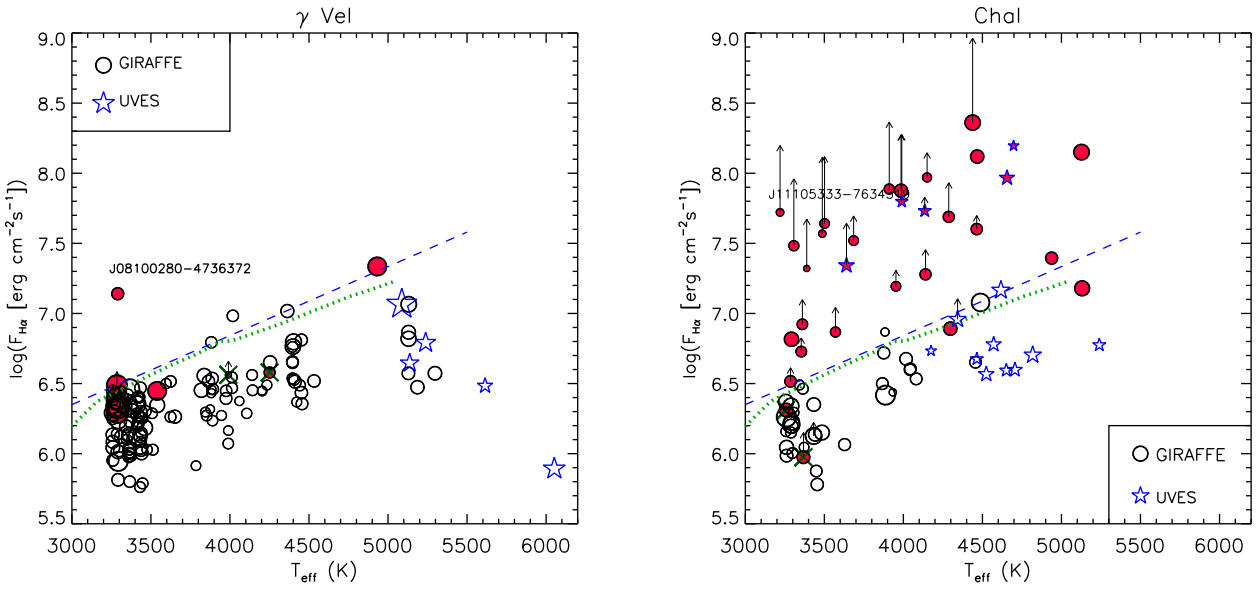

Fig. 11. Hα flux versus $T_{\rm eff}$ for the γ Vel (*left panel*) and the Cha I (*right panel*) members observed with GIRAFFE and UVES. The symbol size scales with the $v \sin i$. The accretor candidates ($10\%W_{\rm H\alpha} > 270$ km s^{-1}) are denoted with filled symbols and typically have a flux larger than the other stars. The candidates that have been rejected on the basis of the $EW_{\rm H\alpha}$ criterion (Sect. 3.5) are marked with crosses. The flux values corrected for veiling by the factor $(1 + r)$ are denoted by arrowheads. In each box, the dashed straight line is drawn to follow the upper envelope of the sources without accretion, while the dotted line is the saturation criterion adopted by Barrado y Navascués & Martín (2003) to separate classical from weak T Tauri.

two boundaries are very close, especially for the coolest stars, where the subtraction of the non-active template has a negligible effect on the $F_{\rm H\alpha}$ due to both the faint photospheric absorption (compared to usually strong line emissions) and the low continuum flux.

The behaviour of $R'_{\rm H\alpha}$ versus $T_{\rm eff}$ for both clusters is displayed in Fig. 12, where a much flatter trend appears. The accretor candidates lie in the upper part of these plots too. The dividing line for this activity index, overplotted with a dashed line, is given by:

$$\log R'_{\rm H\alpha} = -3.4 + 0.00008(T_{\rm eff} - 3000)\,. \quad (9)$$

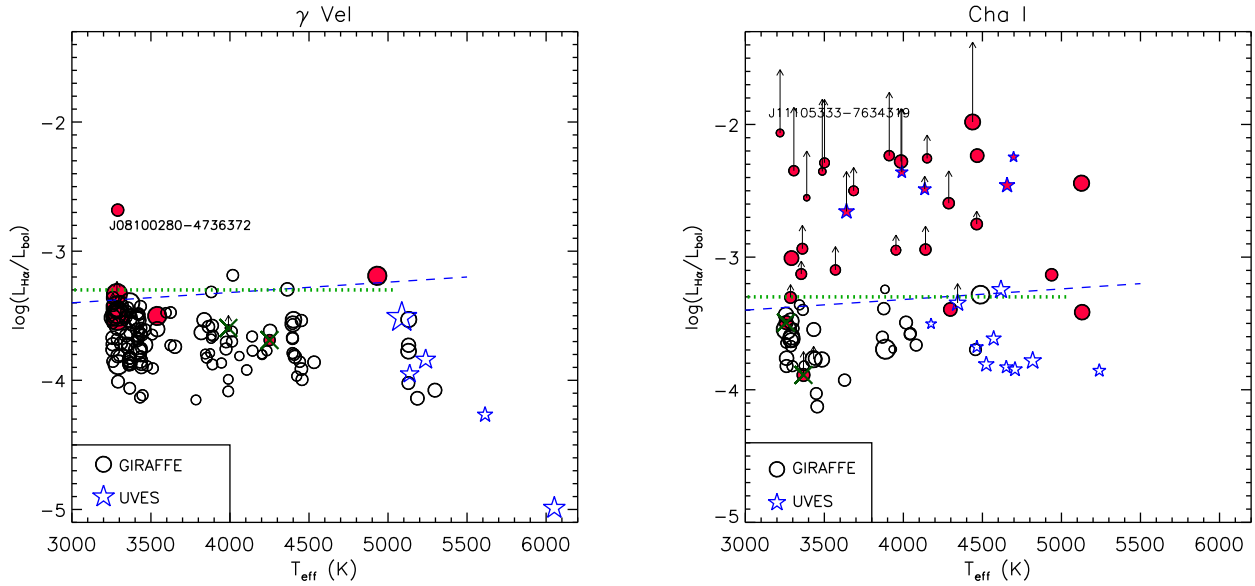

Fig. 12. $R'_{\rm H\alpha}$ versus $T_{\rm eff}$ for the γ Vel (*left panel*) and the Cha I (*right panel*) members observed with GIRAFFE and UVES. The meaning of the symbols, arrowheads, and dashed/dotted lines is as in Fig. 11.

We note that the average value of this line is close to the saturation limit, $\log R'_{\rm H\alpha} = -3.3$, adopted by Barrado y Navascués & Martín (2003) as the boundary between accreting and non-accreting objects, which is also displayed in Fig. 12.

In the case of γ Vel, most stars have $F_{\rm H\alpha}$ close to the maximum values found by Martínez-Arnáiz et al. (2011, see their Fig. 7) for stars with X-ray luminosity in the saturated regime. Moreover, the fluxes do not seem to correlate with the $v \sin i$, as indicated by the Spearman's rank correlation coefficient $\rho = 0.057$ and by the two-sided significance of its deviation from zero $\sigma = 0.519$, even rejecting the few accretors. A higher coefficient ($\rho = 0.452$) with a $\sigma = 7.6 \times 10^{-8}$ is found instead for $\log R'_{\rm H\alpha}$ versus $v \sin i$. This suggests that most stars have already reached the saturation of magnetic activity, while the remaining objects are likely contributing to this residual correlation which is best detected in the $\log R'_{\rm H\alpha}$ diagnostic. Similar results are found for Cha I when the accreting objects are disregarded.

Eight out of the 140 UVES+GIRAFFE members of the γ Vel cluster are accretor candidates ($10\%W_{\rm H\alpha} > 270\,{\rm km\,s^{-1}}$), but we only confirmed three accretors. The percentage of accretors is then 2 % or, at most, 4 % if we consider also the possible accretors. All these objects fall above or close to the dividing line, while two candidates, namely J08103074−4726219 and J08104649−4742216, lie well below this boundary (see Figs. 11 and 12, left panels). The first one has $10\%W_{\rm H\alpha} \sim 280$ km s^{-1} and was finally classified as a non-accretor. The second one shows a large $10\%W_{\rm H\alpha}$ uncertainty ($\sim 30\%$), due to bad quality of the spectrum and cannot be considered as an accretor according to the criteria adopted in Sect. 3.5. Both are reported as Class III sources by Hernández et al. (2008) based on their SED.

All the members of Cha I with $10\%W_{\rm H\alpha} > 270\,{\rm km\,s^{-1}}$ fall above or very close to the dividing line with only two exceptions. One of these two stars is J11085242−7519027 ($T_{\rm eff} \sim 3400$ K, $10\%W_{\rm H\alpha} \sim 272\,{\rm km\,s^{-1}}$), which we finally do not classify as an accretor, while the other, namely J11122441−7637064 ($T_{\rm eff} \sim 5100$ K and $10\%W_{\rm H\alpha} \sim 380\,{\rm km\,s^{-1}}$), is defined as an accretor. Moreover, J11122441−7637064 was previously classified as a classical T Tauri on the basis of *Spitzer* photometry (e.g., Wahhaj et al. 2010) and Nguyen et al. (2012) reported a value of $10\%W_{\rm H\alpha}$ ($381\,{\rm km\,s^{-1}}$) very close to our measurement. Luhman (2007) found a lower effective temperature for it ($T_{\rm eff} \sim 4660$ K) from low-dispersion spectra. If we adopt this temperature, we obtain a flux $\log F_{\rm H\alpha} \simeq 7.0$ (in cgs units) that leads the star slightly closer to the dividing line. However, this star is a visual binary with a companion at about 2″ (Daemgen et al. 2013), whose light could have contaminated the GIRAFFE spectrum.

As mentioned in Sect. 3.1, the veiling was taken as a free parameter only for the stars with a strong and broad Hα emission, which was considered as the main requirement for the pre-selection of accretor candidates within the GES. We found no star in γ Vel with $r > 0.25$. Among the eight stars with a veiling detection, one is an accretor and other two are possible accretors according to our definition in Sect. 3.5.

In Cha I the picture is much different. Among the 74 UVES+GIRAFFE members, 31 sources (about 42 %) display $10\%W_{\rm H\alpha} > 270$ km s^{-1} and all are confirmed (26 sources, i.e. 35 %) or possible (5 sources) accretors. Moreover, most of them lie above the line of non-accreting stars in Fig. 11 by about 0.5–1.0 dex. In addition, as displayed in Fig. 13, all the stars with significant veiling ($r \geq 0.5$) are accretors (see also Sect. 4.4). Figure 13 also shows a positive correlation between Hα flux and r, at least for the objects with $r \geq 0.25$ for which the Spearman's rank analysis yields a coefficient $\rho = 0.58$ with a significance of $\sigma = 0.003$. Presently, a more accurate analysis of the stellar properties versus veiling cannot be done because of the uncertainties of the veiling values for GIRAFFE spectra due to their limited spectral range and the absence of strong photospheric lines in the HR15N setup.

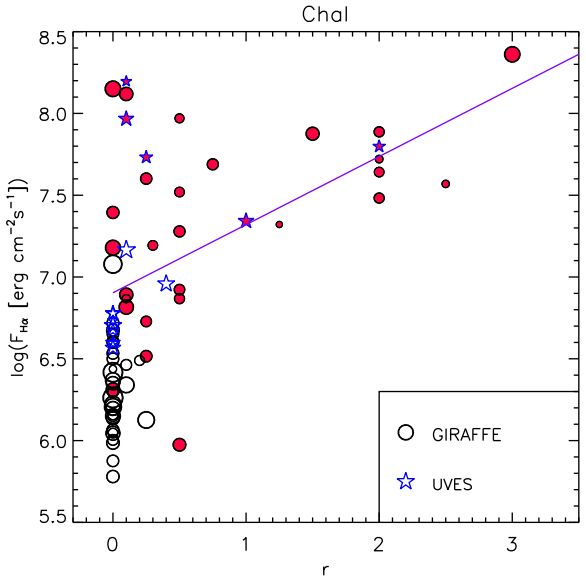

Fig. 13. Hα flux versus veiling for the Cha I members observed with GIRAFFE and UVES. The accretor candidates ($10\%W_{\rm H\alpha} > 270$ km s^{-1}) are denoted by filled symbols, as in Fig. 11. All the stars with a significant veiling ($r \geq 0.5$) turn out to be confirmed or possible accretors. The full line is a linear best fit to the data with $r \geq 0.25$.

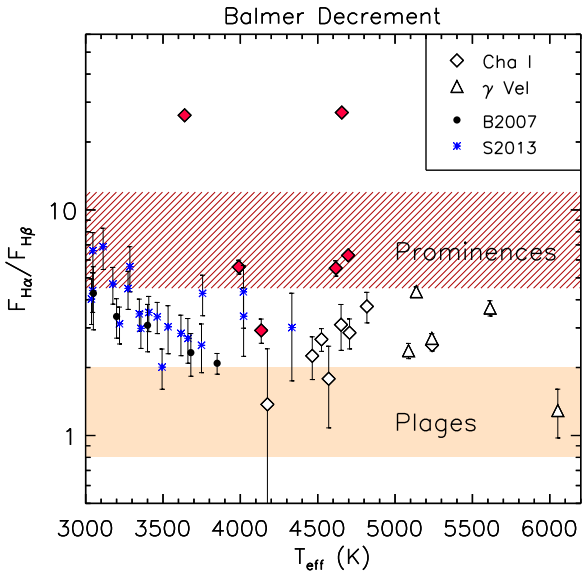

Fig. 14. Balmer decrement ($F_{\rm H\alpha}/F_{\rm H\beta}$) versus effective temperature for the γ Vel (triangles) and Cha I (diamonds) stars with residual emission detected both in the Hα and Hβ lines. The accretors are displayed with filled symbols. The decrements measured for late-K and M-type stars by Bochanski et al. (2007, B2007) and Stelzer et al. (2013, S2013) are overplotted with different symbols. The range of values typical for solar plages and for prominences are also shown by the shaded and hatched areas, respectively.

Concluding, these two clusters are different both in the accretion properties and in the emitted average Hα line flux, with γ Vel showing less accretion signatures than Cha I, as expected due to its older age. In particular, the line flux emitted by the confirmed or possible accreting objects in γ Vel is comparable to, or just larger than, the highest chromospheric fluxes emitted by the other γ Vel members, suggesting that most of these stars are near the end of the accretion phase.

4.3. Balmer decrement

The Hα and Hβ fluxes measured in the UVES spectra allowed us to calculate the Balmer decrement ($F_{\rm H\alpha}/F_{\rm H\beta}$) that is a sensitive indicator of the physical conditions, mainly density and temperature, in the emitting regions. The Balmer decrement for the γ Vel and Cha I members is plotted versus $T_{\rm eff}$ in Fig. 14.

It is well know that the Balmer decrement for the Sun is quite low ($\sim$1–2) in the optically thick plasma of plages or pre-flare active regions, while it is much higher ($\sim$4.5–12) in the prominences (see, e.g. Tandberg-Hanssen 1967; Landman & Mongillo 1979; Chester 1991).

For the very active giants or subgiants in RS CVn binaries, a Balmer decrement in the range 3–10, i.e. significantly larger than that of solar active regions, has been observed. This has been interpreted as the result of different conditions in the active regions or as the combined effect of plage-like and prominence-like structures (Hall & Ramsey 1992; Chester et al. 1994). For active main-sequence stars, a lower Balmer decrement (in the range 2.2–3.2), but still slightly larger than in solar plages, has been observed (see, e.g. Frasca et al. 2010, 2011). In the case of late-K and M-type stars, a Balmer decrement intermediate between solar plages and prominences (2–5), with an increasing trend with the decrease of $T_{\rm eff}$, has been observed both in field dMe stars (Bochanski et al. 2007) and in PMS Class III stars in regions with age of 1–10 Myr (Stelzer et al. 2013). These data are also displayed in Fig. 14 for comparison.

For the few chromospherically active stars members of γ Vel and for the non-accreting stars in Cha I we also found a Balmer decrement between about 2 and 5, i.e. intermediate between solar plages and prominences. This suggests either that the chromospheric active regions of these young stars have a different structure, mainly as regards their optical thickness, compared to the solar plages or that the emitted chromospheric flux is the results of contributions from plage-like and prominence-like regions, the latter having a much higher Balmer decrement. Moreover, these data do not show any clear dependence of the Balmer decrement on $T_{\rm eff}$ for the G–K-type stars in 1–10 Myr age range, unlike what is seen for M-type stars (Stelzer et al. 2013).

The star J11064510−7727023 (=UX Cha) was disregarded in this analysis because of unreliable $EW_{\rm H\beta}$ value due to extremely low S/N of the spectrum in the Hβ region. The six accreting stars in Cha I observed with UVES display instead higher Balmer decrements, from about 3 to 30, as expected from an optically thin accreting matter.

4.4. Mass accretion rate

In Fig. 15, the mass accretion rates measured by means of the $10\%W_{\rm H\alpha}$ and $EW_{\rm H\alpha}$ diagnostics are plotted as a function of the stellar mass derived from the HR diagram (see Sect. 3.3). From this figure, it is evident how all con-

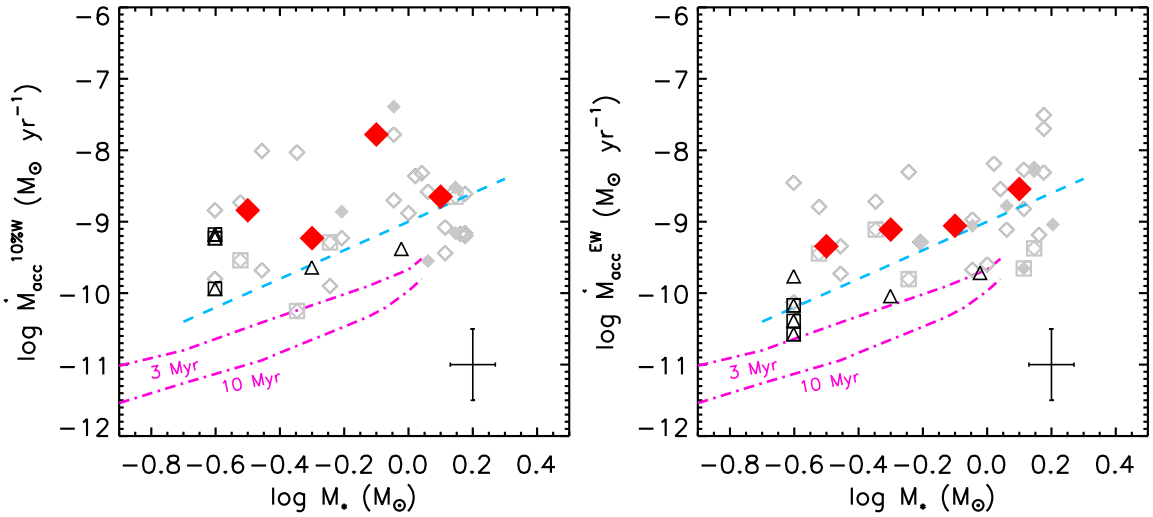

Fig. 15. Mass accretion rate from $10\%W_{\rm H\alpha}$ (*left panel*) and $EW_{\rm H\alpha}$ (*right panel*) versus stellar mass. Diamonds and triangles represent Cha I and γ Vel stars, where filled and empty symbols refer to UVES and GIRAFFE data, respectively. Squares mark the position of the possible accretors. Big red diamonds represent the median values of $\dot{M}_{\rm acc}$ for stellar masses of Cha I members binned at $0.2M_\odot$, where both confirmed and possible accretors were considered. The dashed line represents the $\dot{M}_{\rm acc} \propto M_\star^2$ relation, while the "noise boundaries" at 3 Myr and 10 Myr due to chromospheric activity are overplotted by dash-dotted lines (Manara et al. 2013). Mean error bars are overplotted on the right corners of both panels.

firmed and possible accretors in both clusters fall above the boundaries between chromospheric emission and accretion as defined by Manara et al. (2013) for the ages of Cha I and γ Vel ($\sim$ 3 Myr and $\sim$ 10 Myr, respectively). This means that the selection of accreting objects within the GES is reliable.

Moreover, from the same figure, it is also evident the large spread in accretion rates for any given mass similar to what already found by previous studies. Short-term (e.g., Biazzo et al. 2012) and long-term variability (up to $\sim$0.5 dex according to Costigan et al. 2014) may contribute to, but do not explain the large vertical spread of the $\dot{M}_{\rm acc} - M_\star$ relationship. Different methodologies to derive $\dot{M}_{\rm acc}$ (see, e.g., Alcalá et al. 2014) may also contribute to the scatter, but the large spread (up to 3 dex) observed in the $\dot{M}_{\rm acc} - M_\star$ relation is still unexplained. What seems to be reached is the general agreement in finding a dependence of $\dot{M}_{\rm acc}$ on stellar mass with a power of $\sim$ 2 (e.g., Muzerolle et al. 2005; Herczeg & Hillenbrand 2008; Alcalá et al. 2014). From Fig. 15, despite the large spread in $\dot{M}_{\rm acc}$ at each stellar mass, an increasing trend of $\dot{M}_{\rm acc}$ with $M_\star$ seems to be present, and this emerges more clearly when $\dot{M}_{\rm acc}$ is derived from $EW_{\rm H\alpha}$. The power-law relation $\dot{M}_{\rm acc} \propto M_\star^2$, which is also depicted in Fig. 15, is not inconsistent with our data, although the scatter does not allow us to say more. A Spearman's rank correlation analysis yields for Cha I a coefficient $\rho = 0.44$ with a significance $\sigma = 0.01$ for $\dot{M}_{\rm acc}$ derived from $EW_{\rm H\alpha}$, indicating a significant positive correlation, while $\dot{M}_{\rm acc}$ is less correlated with the stellar mass ($\rho = 0.26$, $\sigma = 0.16$) when it is obtained from $10\%W_{\rm H\alpha}$.

Summarizing, the mass accretion rate for the few accretors in the γ Vel sample ranges from $\sim 10^{-11}$ to $10^{-9} M_\odot\,{\rm yr}^{-1}$, while for the Cha I members it is in the range $10^{-10} - 5 \times 10^{-8}\ M_\odot\,{\rm yr}^{-1}$, with a mean value of $\sim 2 \times 10^{-9} M_\odot\,{\rm yr}^{-1}$ at $\sim 1 M_\odot$. Considering the different ages of γ Vel and Cha I, these values are consistent with the temporal decay of mass accretion rates due to the mechanisms driving the evolution and dispersal of circumstellar disks (see, e.g., Hartmann et al. 1998). Moreover, as mentioned in Sect. 4.2, we find a fraction of accretors of $\sim 35 - 42\%$ in Cha I and $\sim 2 - 4\%$ in γ Vel, which are in very good agreement with the results of Fedele et al. (2010) based on low resolution spectra and consistent with the disk fractions for stellar clusters with ages similar to that of γ Vel and Cha I (Ribas et al. 2014).

A comparison between our mass accretion rates with those derived in the literature is presented in Appendix A.

5. Summary and Conclusions

In this paper we used the dataset provided by the GES consortium to study the chromospheric activity and accretion properties of the γ Vel and Cha I regions. Our findings can be summarized as follows:

- GIRAFFE spectra acquired within the GES survey with a $S/N > 20$ for stars in the young associations γ Vel and Cha I form statistically significant samples for the analysis of $v \sin i$.
- The $v \sin i$ distribution for the members of γ Vel appears asymmetric with a main peak at about 10 km s^{-1} and a broad tail extending towards fast rotators. This suggests the presence of both stars that are at the end of the disk-locking phase and are still rotating rather slowly and others that have started to spin-up while contracting and approaching the ZAMS. Some indication of a distinction between the A and B kinematical

subsamples discovered by Jeffries et al. (2014) emerges from the $v \sin i$ data.

- We found no clear dependence of the chromospheric Hα flux on $v \sin i$. Only a hint of correlation with the $v \sin i$ emerges instead for $\log R'_{\rm H\alpha}$, i.e. the line flux normalized to the bolometric one. This very weak dependence on $v \sin i$ may be due to activity saturation for most of the non-accreting stars, as witnessed by the high chromospheric fluxes that are comparable to those typical for stars in the saturated regime.
- A low fraction ($\sim 2-4\%$) of γ Vel members display mass accretion, while a much larger percentage ($\sim 35-42\%$) was found for Cha I. This is an expected result on the basis of the quick dissipation of the disks after their typical lifetime of 5–7 Myr and suggests that γ Vel is right at the end of the accretion phase.
- Accreting and active stars occupy two different regions in a $T_{\rm eff}$–$F_{\rm H\alpha}$ diagram and we propose a simple criterion for distinguishing them, which is, however, well consistent with previous findings (e.g., Barrado y Navascués & Martín 2003). The few stars around the dividing line in our plots are possibly near the end of their accretion phase or have very high chromospheric fluxes.
- The Balmer decrement ($F_{\rm H\alpha}/F_{\rm H\beta}$) was calculated for the stars observed with UVES, where the setup included both Hα and Hβ. In the case of the active stars in γ Vel and the non-accreting members of Cha I, we found values in the range 2–5, that are slightly larger than those observed in solar plages, as already found in other very active stars. This indicates either that the chromospheric active regions are not as optically thick as in the Sun or that the hemisphere averaged chromospheric emission is the result of a "mixture" of plage-like and prominence-like regions, the latter having a much higher Balmer decrement. All the few accreting stars in Cha I observed with UVES display a Balmer decrement of ∼5–30, indicating an optically thin emission from the accreting matter.
- The accreting stars in Cha I display a wide range of r values, but all the stars for which we found a veiling larger than 0.25 are accretors.
- On the one hand, the luminosity in the Hα line proves itself to be a diagnostic more reliable than the Hα 10% width to derive the mass accretion rate, as found in previous works. On the other hand, the Hα 10% width represents a fast and efficient criterion to select accretor candidates for an ad-hoc analysis, e.g. by searching for the value of veiling that, in combination with that of other free parameters, best matches the observations.

Concluding, the results presented in this work, which are based on the first two young clusters observed by the GES, show the huge potential of the survey for the study of fundamental properties of PMS stars, such as their rotation, magnetic activity, and mass accretion properties as a function of basic stellar parameters like mass and age. This type of analysis can be extended to the other young clusters that are being observed within the GES. This will provide an unprecedented picture of these phenomena in low-mass stars during the first stages of their evolution.

Acknowledgements. The authors are grateful to the referee for carefully reading the paper and for her/his useful remarks. This work was partly supported by the European Union FP7 programme through ERC grant number 320360 and by the Leverhulme Trust through grant RPG-2012-541. We acknowledge the support from INAF and Ministero dell'Istruzione, dell' Università e della Ricerca (MIUR) in the form of the grant "Premiale VLT 2012". The results presented here benefit from discussions held during the Gaia-ESO workshops and conferences supported by the ESF (European Science Foundation) through the GREAT Research Network Programme. S.G.S. acknowledge the support from the Fundação para a Ciência e Tecnologia, FCT (Portugal) in the form of the fellowship SFRH/BPD/47611/2008. This research made also use of the SIMBAD database, operated at the CDS (Strasbourg, France) and of the Deep Near Infrared Survey of the Southern Sky (DENIS) database.

References

Alcalá, J. M., Natta, A., Manara, C., et al. 2014, A&A, 561, A2
Antoniucci, S., García-López, R., Nisini, B., et al. 2011, A&A, 534, 32
Baraffe, I., Chabrier, G., Allard, F., & Hauschildt, P. H. 1998, A&A, 337, 403
Bayo, A., Barrado, D., Huélamo, N., et al. 2012, A&A, 547, A80
Barrado y Navascués, D., Martín, E. L. 2003, AJ, 126. 2997
Biazzo, K., Alcalá, J. M., Covino, E., et al. 2012, A&A, 547, A104
Biazzo, K., Alcalá, J. M., Frasca, A., et al. 2014, A&A, 572, A84
Bochanski, J. J., West, A. A., Hawley, S. L., & Covey, K. R. 2007, AJ, 133, 531
Bouvier, J., Forestini, M., & Allain, S. 1997, A&A, 326, 1023
Bragaglia, A., Alfaro, E., Flaccomio, E., et al. 2014, A&A, in preparation
Calvet, N., Briceno, C., Hernández, J., et al. 2005, AJ, 129, 935
Chester, M. M. 1991, Ph. D. Thesis, Pennsylvania State Univ.
Chester, M. M., Hall, J. C., & Buzasi, D. 1994, in Eigth Cambridge Workshop on Cool Stars Slettar Systems and the Sun, ed. J.-P. Caillault, ASP Conf. Ser., 64, 1994
Costigan, G., Scholz, A., Stelzer, B., et al. 2012, MNRAS, 427, 1344
Costigan, G., Vink, J. K., Scholz, A., Ray, T., & Testi, L. 2014, MNRAS, 440, 3444
Daemgen, S., Petr-Gotzens, M. G., Correia, S., et al. 2013, A&A, 554A, 43
Espaillat, C., Furlan, E., D'Alessio, P., et al. 2011, A&A, 728, 49
Fang, M., van Boekel, R., Wang, W., et al. 2009, A&A, 504, 461
Fedele, D., van den Ancker, M. E., Henning, Th., Jayawardhana, R., & Oliveira, J. M. 2010, A&A, 510, A72
Frasca, A., & Catalano, S. 1994, A&A, 284, 883
Frasca, A., Alcalà, J. M., Covino, E., et al. 2003, A&A, 405, 149
Frasca, A., Guillout, P., Marilli, E., et al. 2006, A&A, 454, 301
Frasca, A., Covino, E., Spezzi, L., et al. 2009, A&A, 508, 1313
Frasca, A., Biazzo, K., Kővári, Zs., Marilli, E., & Çakırlı, Ö. 2010, A&A, 518, 48
Frasca, A., Fröhlich, H.-E., Bonanno, A., et al. 2011, A&A, 532, 81
Gilmore, G., Randich, S., Asplund, M., et al. 2012, The Messenger, 147, 25
Jeffries, R. D., Naylor T., Walter F. M., Pozzo M. P., & Devey C. R. 2009, MNRAS, 393, 538
Jeffries, R. D., Jackson R. J., Cottaar M., et al. 2014, A&A, 563, A94
Hall, J. C., & Ramsey, L. W. 1992, AJ, 104, 1942
Herbst, W., Bailer-Jones, C. A. L., Mundt, R., Meisenheimer, K., & Wackermann, R. 2002, A&A, 396, 513
Haisch, K. E., Lada, E. A., & Lada, C. J. 2001, ApJ, 553, 153
Hartmann, L. 1998, in Accretion Processes in Star Formation, Cambridge Univ. Press
Hartmann, L., Calvet, N., Gullbring, E., & D'Alessio, P. 1998, ApJ, 495, 385
Hauschildt, P. H., Allard, F., & Baron, E. 1999, ApJ, 512, 377
Herczeg, G. J., & Hillenbrand, L. A. 2008, ApJ, 681, 594
Hernández J., Hartmann L., Calvet N., et al. 2008, ApJ, 686, 1195
Kim, K. H., Watson, D. M., Manoj, P., et al. 2009, ApJ, 700, 1017
Kraus, A. L., Shkolnik, E. L., Allers, K. L., &, Liu, M. C. 2014, AJ, 147, 146
Ingleby, L., Calvet, N., Herczeg, G., et al. 2013, ApJ, 767, 112
Lada, C. J., Muench, A. A., Luhman, K. L., et al. 2006, AJ, 131, 1574
Landman, D. A & Mongillo, M. 1979, ApJ, 230, 581
Lanzafame, A. C., Frasca, A., Damiani, F., et al. 2014, A&A, submitted
Luhman, K. L. 2007, ApJ, 173, 104
Luhman, K. L. 2008, in Handbook of Star Forming Regions Vol. II, ed. B. Reipurth, ASP Mon. Publ., 169

Luhman, K. L., Allen, L. E., Allen, P. R., et al. 2008, ApJ, 675, 1375
Mamajek, E. E., & Hillenbrand L. A. 2008, ApJ, 687, 1264
Manara, C., Testi, L., Rigliaco, E., et al. 2013, A&A, 551, A107
Manoj, P., Kim, K. H., Furlan, E., et al. 2001, ApJS, 193, 11
Martínez-Arnáiz, R., et al. 2011, MNRAS, 414, 2629
Meibom, S., Mathieu, R. D., & Stassun, K. G. 2009, ApJ, 695, 679
Messina, S., Desidera, S., Turatto, M., Lanzafame, A. C., & Guinan, E. F. 2010, A&A, 520, 15
Messina, S., Pizzolato, N., Guinan, E. F., & Rodonò, M. 2003, A&A, 410, 671
Montes, D., et al. 1995, A&AS, 114, 287
Moultaka, J., Ilovaisky, S. A., Prugniel, P., & Soubiran, C. 2004, PASP, 116, 693
Muzerolle, J., Luhman, K. L., Briceño, C., Hartmann, L., & Calvet, N. 2005, ApJ, 625, 906
Natta, A., Testi, L., Muzerolle, J., et al. 2004, A&A, 424, 603
Nguyen, D. C., Brandeker, A., van Kerkwijk, M. H., & Jayawardhana R. 2012, ApJ, 745, 119
Pace, G. 2013, A&A, 551, L8
Pace, G., & Pasquini, L. 2004, A&A, 426, 1021
Pecaut, M. J., & Mamajek, E. E. 2013, ApJS, 208, 9
Pizzolato, N., Maggio, A., Micela, G., Sciortino, S., & Ventura, P. 2003, A&A, 397, 147
Pozzo, M., Jeffries, R. D., Naylor, T., et al. 2000, MNRAS, 313L, 23
Preibisch, T., & Feigelson, E. D. 2005, ApJS, 160, 390
Press, W. H., Teukolsky, S. A., Wetterling, W. T., & Flannery, B. P. 1992, Numerical Recipes, The Art of Scientific Computing (Cambridge University Press), second edition
Randich, S., Gilmore, G., & Gaia-ESO Consortium 2013, The Messenger, 154, 47
Rebull, L. M., Wolff, S. C., Strom, S. E., & Makidon, R. B. 2002, AJ, 124, 546
Ribas, A., Merín, B., Bouy, H., Maud, L. T. 2014, å, 561, 54
Robberto, M., Spina, L., Da Rio, N., et al. 2012, AJ, 144, 83
Sacco, G. G., Morbidelli, L., Franciosini, E., et al. 2014, A&A, 565, A113
Sicilia-Aguilar, A., Hartmann, L., Calvet, N., et al. 2006, ApJ, 638, 897
Skumanich A. 1972, ApJ, 171, 265
Soderblom, D. R., Duncan, D. K., & Johnson, D. R. H. 1991, ApJ, 375, 722
Spada, F., Lanzafame, A. C., Lanza, A. F., Messina, S., & Collier Cameron, A. 2011, MNRAS, 416, 447
Spina, L., Randich, S., Palla, F., et al. 2014a, A&A, 567, A55
Spina, L., Randich, S., Palla, F., et al. 2014b, A&A, 568, A2
Stauffer, J. R., Hartmann, L. W., Prosser, C. F., et al. 1997, ApJ, 479, 776
Stelzer, B., Frasca, A., Alcalà, J. M., et al. 2013, A&A, 558, A141
Skrutskie, M. F., Cutri, R. M., Stiening, R., et al. 2006, AJ, 131, 1163
Tandberg-Hanssen, E. 1967, Solar activity, Waltham, Mass.: Blaisdell
Wahhaj, Z., Cieza, L., Koerner, D. W., et al. 2010, ApJ, 724, 835
White, R. J., Basri, G. 2003, ApJ, 582, 1109
Whittet, D. C. B., Prusti, T., Franco, G. A. P., et al. 1997, A&A, 327, 1194
Zacharias, N., Monet, D. G., Levine, S. E., et al. 2004, *American Astron. Soc. Meeting*, 205, #4815; *Bulletin of the American Astronomical Society*, Vol. 36, p.1418
de Zeeuw, P. T., Hoogerwerf, R., de Bruijne, J. H. J., Brown, A. G. A., & Blaauw, A. 1999, ApJ, 117, 399

[1] INAF - Osservatorio Astrofisico di Catania, via S. Sofia 78, 95123, Catania, Italy e-mail: antonio.frasca@oact.inaf.it
[2] Dipartimento di Fisica e Astronomia, Sezione Astrofisica, Università di Catania, via S. Sofia 78, 95123, Catania, Italy
[3] INAF - Osservatorio Astronomico di Capodimonte, via Moiariello 16, 80131, Naples, Italy
[4] INAF - Osservatorio Astronomico di Palermo, Piazza del Parlamento 1, 90134, Palermo, Italy
[5] INAF - Osservatorio Astrofisico di Arcetri, Largo E. Fermi 5, 50125, Firenze, Italy
[6] Astrophysics Group, Keele University, Keele, Staffordshire ST5 5BG, United Kingdom
[7] Departamento de Astrofísica y Ciencias de la Atmósfera, Universidad Complutense de Madrid, 28040 Madrid, Spain
[8] Instituto de Astrofísica de Andalucía, CSIC, Apdo 3004, 18080, Granada, Spain
[9] School of Physics, Astronomy & Mathematics, University of Hertfordshire, College Lane, Hatfield, Hertfordshire, AL10 9AB, United Kingdom
[10] Dipartimento di Fisica e Chimica, Università di Palermo, Piazza del Parlamento 1, 90134, Palermo, Italy
[11] Centro de Astrofísica, Universidade do Porto, Rua das Estrelas 4150-752, Porto, Portugal
[12] S. D. Astronoma y Geodesia, Facultad de Ciencias Matemáticas, Universidad Complutense de Madrid, 28040 Madrid, Spain
[13] European Southern Observatory, Karl-Schwartzschild-Strasse 2, 85748, Garching bei München, Germany
[14] Departamento de Física e Astronomia, Faculdade de Ciências, Universidade do Porto, Rua do Campo Alegre, 4169-007 Porto, Portugal
[15] Institute of Astronomy, University of Cambridge, Madingley Road, Cambridge CB3 0HA, United Kingdom
[16] INAF - Osservatorio Astronomico di Bologna, via Ranzani 1, 40127, Bologna, Italy
[17] Max-Planck Institut für Astronomie, Königstuhl 17, 69117, Heidelberg, Germany
[18] Instituto de Física y Astronomía, Facultad de Ciencias, Universidad de Valparaíso, Av. Gran Bretaña 1111, Playa Ancha, Valparaíso, Chile
[19] Laboratoire Lagrange (UMR7293), Université de Nice Sophia Antipolis, CNRS, Observatoire de la Côte d'Azur, CS 34229, F-06304 Nice cedex 4, France

Table 2. Parameters of the γ Vel members used for this study.

2MASS	RA			DEC			RV	SpT	$T_{\rm eff}$	err	$v \sin i$	err	$EW_{\rm H\alpha}$	err	$F_{\rm H\alpha}$	err	r	err	$10\%W_{\rm H\alpha}$	err	L	err	$M_\star$	$\dot{M}_{\rm acc}^{10\%W}$	$\dot{M}_{\rm acc}^{EW}$
	hh	mm	ss	°	′	″	(km s^{-1})		(K)		(km s^{-1})		(Å)		(erg cm^{-2}s^{-1})				(km s^{-1})		($L_\odot$)		($M_\odot$)	($M_\odot$ yr^{-1})	
GIRAFFE																									
08064390-4731532	08	06	43.90	−47	31	53.2	16.385	M4V	3259	60	15.0	0.5	3.406	0.166	8.967×10^{5}	1.482×10^{5}	0.00	0.00	105.10	0.00	0.0743	0.0135	0.25	...	...
08065469-4657241	08	06	54.69	−46	57	24.1	19.149	K0V	5131	65	33.7	1.6	2.468	0.119	1.163×10^{7}	8.510×10^{5}	0.00	0.00	206.85	21.00	1.3081	0.2279	1.15	...	...
08070036-4745250	08	07	00.36	−47	45	25.0	15.359	M4V	3293	95	65.5	9.4	3.078	0.275	8.809×10^{5}	2.276×10^{5}	0.00	0.00	205.70	0.00	0.0685	0.0139	0.25	...	...
08071155-4719512	08	07	11.55	−47	19	51.2	17.674	K5V	4202	143	6.7	3.9	1.796	0.146	2.812×10^{6}	7.144×10^{5}	0.00	0.00	136.00	8.06	0.3559	0.0766	1.00	...	...
08072198-4711230	08	07	21.98	−47	11	23.0	20.369	M4V	3287	95	57.1	6.0	7.641	0.436	2.156×10^{6}	5.399×10^{5}	0.10	0.10	201.10	0.00	0.1189	0.0241	0.25	...	...
08072538-4728178	08	07	25.38	−47	28	17.8	18.354	M4V	3291	95	45.0	0.5	8.245	0.473	2.349×10^{6}	5.862×10^{5}	0.00	0.00	164.50	0.00	0.0460	0.0093	0.25	...	...
08073251-4734419	08	07	32.51	−47	34	41.9	20.971	M1V	3784	110	8.3	3.8	1.111	0.121	8.207×10^{5}	1.906×10^{5}	0.00	0.00	120.00	4.81	0.1344	0.0273	0.70	...	...
08073363-4703355	08	07	33.63	−47	03	35.5	16.525	K5V	4143	186	11.4	2.6	1.985	0.071	2.831×10^{6}	9.188×10^{5}	0.00	0.00	145.10	8.06	0.2111	0.0517	0.80	...	...
08073420-4725072	08	07	34.20	−47	25	07.2	19.688	K8V	3882	221	13.2	2.7	7.051	0.219	6.224×10^{6}	2.645×10^{6}	0.00	0.00	156.60	11.31	0.2354	0.0664	0.85	...	...
08073442-4654016	08	07	34.42	−46	54	01.6	17.137	M4V	3308	85	15.1	2.5	10.265	0.306	2.763×10^{6}	5.644×10^{5}	0.00	0.00	128.00	0.00	0.0482	0.0094	0.25	...	...
08074304-4711071	08	07	43.04	−47	11	07.1	19.506	M4V	3864	221	16.6	1.8	3.840	0.107	3.285×10^{6}	1.398×10^{6}	0.00	0.00	142.85	1.63	0.1389	0.0393	0.75	...	...
08074361-4722095	08	07	43.61	−47	22	09.5	17.204	K5V	4396	233	11.9	2.5	1.617	0.088	3.442×10^{6}	1.138×10^{6}	0.00	0.00	125.70	0.00	0.3872	0.1044	0.95	...	...
08074648-4711496	08	07	46.48	−47	11	49.6	19.182	M4V	3299	95	12.9	1.6	3.594	0.135	1.043×10^{6}	2.540×10^{5}	0.00	0.00	162.30	0.00	0.0560	0.0113	0.25	...	...
08074909-4744364	08	07	49.09	−47	44	36.4	16.022	M4V	3476	92	10.2	1.8	2.692	0.158	1.068×10^{6}	2.279×10^{5}	0.00	0.00	115.40	14.57	0.0880	0.0174	0.40	...	...
08075314-4726322	08	07	53.14	−47	26	32.2	18.641	M4V	3430	77	8.9	2.9	7.053	0.216	2.528×10^{6}	4.447×10^{5}	0.00	0.00	125.70	3.25	0.0935	0.0177	0.40	...	...
08075546-4707460	08	07	55.46	−47	07	46.0	19.887	K3V	4363	149	20.5	1.4	4.734	0.092	1.040×10^{7}	1.942×10^{6}	0.00	0.00	196.50	0.00	0.7777	0.1676	1.30	...	...
08075757-4743462	08	07	57.57	−47	43	46.2	17.106	K5V	4402	233	36.7	2.9	2.923	0.126	6.274×10^{6}	2.056×10^{6}	0.00	0.00	169.15	16.19	0.3014	0.0812	0.85	...	...
08080314-4741495	08	08	03.14	−47	41	49.5	21.303	K5V	4442	349	12.8	2.9	1.354	0.088	3.075×10^{6}	1.435×10^{6}	0.00	0.00	130.30	16.12	0.2215	0.0788	0.75	...	...
08080388-4720433	08	08	03.88	−47	20	43.3	16.654	M4V	3624	356	13.6	1.8	6.037	0.178	3.277×10^{6}	2.449×10^{6}	0.00	0.00	133.70	11.31	0.1602	0.0684	0.57	...	...
08080774-4659130	08	08	07.74	−46	59	13.0	19.271	K8V	3882	74	7.6	1.8	3.232	0.109	2.855×10^{6}	4.035×10^{5}	0.00	0.00	116.60	0.00	0.1665	0.0305	0.80	...	...
08080881-4732336	08	08	08.81	−47	32	33.6	16.914	M4V	3624	356	12.1	3.5	3.369	0.102	1.829×10^{6}	1.367×10^{6}	0.00	0.00	115.40	8.06	0.1351	0.0576	0.57	...	...
08080943-4732250	08	08	09.43	−47	32	25.0	17.262	M4V	3342	169	18.9	1.6	5.370	0.111	1.572×10^{6}	6.329×10^{5}	0.00	0.00	131.45	1.63	0.1864	0.0489	0.30	...	...
08081498-4715380	08	08	14.98	−47	15	38.0	18.975	K8V	4012	150	11.2	1.6	3.134	0.095	3.511×10^{6}	9.750×10^{5}	0.00	0.00	145.10	46.81	0.1689	0.0378	0.80	...	...
08081723-4740092	08	08	17.23	−47	40	09.2	20.253	K5V	4452	348	17.3	1.6	1.182	0.123	2.721×10^{6}	1.275×10^{6}	0.00	0.00	134.80	0.00	0.4096	0.1451	0.95	...	...
08082021-4720259	08	08	20.21	−47	20	25.9	16.311	M4V	3258	60	21.0	0.5	5.201	0.211	1.366×10^{6}	2.228×10^{5}	0.00	0.00	121.10	0.00	0.0856	0.0156	0.25	...	...
08082846-4716020	08	08	28.46	−47	16	02.0	17.754	K5V	4411	232	19.5	1.8	1.501	0.089	3.264×10^{6}	1.067×10^{6}	0.00	0.00	132.60	3.25	0.3686	0.0989	0.95	...	...
08083827-4745000	08	08	38.27	−47	44	60.0	16.270	M3V	3367	154	19.8	1.8	3.527	0.187	1.093×10^{6}	4.000×10^{5}	0.00	0.00	118.80	0.00	0.0567	0.0140	0.30	...	...
08083838-4728187	08	08	38.38	−47	28	18.7	25.000	K1V	4932	232	57.0	3.5	5.501	0.242	2.164×10^{7}	4.882×10^{6}	0.00	0.00	362.25	1.63	0.5703	0.1433	0.95	−9.38	−9.72
08084469-4706591	08	08	44.69	−47	06	59.1	16.548	M4V	3426	184	12.0	0.5	5.251	0.122	1.862×10^{6}	7.806×10^{5}	0.00	0.00	154.30	8.06	0.1420	0.0386	0.40	...	...
08084700-4739180	08	08	47.00	−47	39	18.0	20.629	M4V	3366	154	13.9	1.8	2.044	0.110	6.320×10^{5}	2.315×10^{5}	0.00	0.00	115.45	24.25	0.0878	0.0217	0.30	...	...
08084743-4742349	08	08	47.43	−47	42	34.9	17.417	M4V	3292	95	24.5	1.6	3.984	0.285	1.032×10^{6}	2.492×10^{5}	0.00	0.00	173.55	9.83	0.1984	0.0402	0.30	...	...
08084881-4653424	08	08	48.81	−46	53	42.4	15.640	M4V	3652	373	20.2	2.9	3.194	0.094	1.835×10^{6}	1.437×10^{6}	0.00	0.00	142.85	1.63	0.2594	0.1145	0.62	...	...
08085117-4716075	08	08	51.17	−47	16	07.5	17.368	K5V	4396	233	14.9	2.5	2.095	0.114	4.459×10^{6}	1.474×10^{6}	0.00	0.00	129.10	8.06	0.2537	0.0684	0.80	...	...
08085214-4722579	08	08	52.14	−47	22	57.9	16.359	K5V	4203	116	8.0	3.8	1.779	0.131	2.794×10^{6}	5.828×10^{5}	0.00	0.00	131.45	14.64	0.2853	0.0570	0.90	...	...
08085391-4715075	08	08	53.91	−47	15	07.5	17.215	K8V	4018	150	13.8	1.7	8.477	0.152	9.617×10^{6}	2.648×10^{6}	0.00	0.00	246.80	8.22	0.1939	0.0434	0.80	...	...
08085400-4717236	08	08	54.00	−47	17	23.6	16.752	K8V	3989	63	10.9	1.7	1.100	0.068	1.180×10^{6}	1.593×10^{5}	0.00	0.00	121.15	35.57	0.2639	0.0470	0.90	...	...
08090157-4717069	08	09	01.57	−47	17	06.9	20.726	M4V	3595	186	9.8	1.6	6.183	0.216	3.162×10^{6}	1.226×10^{6}	0.00	0.00	150.85	16.19	0.0869	0.0231	0.57	...	...
08090379-4742157	08	09	03.79	−47	42	15.7	16.791	M1V	3893	233	11.9	2.5	3.203	0.110	2.881×10^{6}	1.290×10^{6}	0.00	0.00	113.10	8.06	0.1658	0.0484	0.80	...	...
08090758-4718422	08	09	07.58	−47	18	42.2	17.743	K5V	4395	233	14.9	2.5	2.130	0.124	4.528×10^{6}	1.501×10^{6}	0.00	0.00	137.10	3.25	0.4692	0.1266	1.05	...	...
08090875-4707441	08	09	08.75	−47	07	44.1	16.806	M4V	3358	181	47.7	13.9	7.190	0.246	2.183×10^{6}	9.415×10^{5}	0.00	0.00	156.55	4.88	0.0621	0.0169	0.30	...	...
08090915-4745105	08	09	09.15	−47	45	10.5	19.999	M3V	3369	154	21.3	2.5	3.141	0.172	9.777×10^{5}	3.578×10^{5}	0.00	0.00	107.40	0.00	0.0688	0.0170	0.30	...	...
08090978-4726305	08	09	09.78	−47	26	30.5	15.850	M3V	3363	154	17.5	1.6	3.518	0.142	1.080×10^{6}	3.943×10^{5}	0.00	0.00	100.60	0.00	0.0671	0.0166	0.30	...	...
08091002-4726342	08	09	10.02	−47	26	34.2	14.132	M4V	3288	95	96.6	18.7	8.644	0.530	2.445×10^{6}	6.141×10^{5}	0.00	0.00	240.00	0.00	0.0827	0.0168	0.25	...	...
08091036-4720250	08	09	10.36	−47	20	25.0	16.317	M1V	3837	196	26.3	1.6	4.428	0.079	3.606×10^{6}	1.346×10^{6}	0.00	0.00	138.30	11.31	0.2859	0.0754	0.85	...	...
08091392-4715498	08	09	13.92	−47	15	49.8	15.470	M4V	3417	184	16.9	1.8	4.682	0.116	1.624×10^{6}	6.844×10^{5}	0.00	0.00	116.55	6.43	0.1332	0.0363	0.35	...	...
08091543-4726105	08	09	15.43	−47	26	10.5	23.045	M4V	3293	95	43.7	8.6	6.033	0.340	1.727×10^{6}	4.298×10^{5}	0.00	0.00	160.00	0.00	0.0827	0.0168	0.25	...	...
08091748-4715558	08	09	17.48	−47	15	55.8	18.316	M4V	3421	171	17.2	1.8	8.970	0.190	2.530×10^{6}	8.689×10^{5}	0.00	0.00	156.55	1.63	0.2216	0.0577	0.40	...	...
08091846-4718420	08	09	18.46	−47	18	42.0	16.396	M4V	3358	154	13.0	1.6	3.149	0.078	9.563×10^{5}	3.484×10^{5}	0.00	0.00	121.10	12.87	0.1789	0.0443	0.35	...	...
08091979-4720483	08	09	19.79	−47	20	48.3	18.281	M1V	3844	53	8.3	1.6	2.397	0.096	1.980×10^{6}	2.064×10^{5}	0.00	0.00	104.00	11.31	0.1426	0.0250	0.75	...	...
08092183-4735370	08	09	21.83	−47	35	37.0	19.604	M4V	3259	60	23.4	1.6	4.196	0.206	1.105×10^{6}	1.827×10^{5}	0.00	0.00	125.70	0.00	0.0452	0.0082	0.20	...	...
08092234-4717333	08	09	22.34	−47	17	33.3	13.382	M4V	3258	60	19.6	1.8	4.630	0.274	1.216×10^{6}	2.051×10^{5}	0.00	0.00	132.50	0.00	0.0574	0.0105	0.20	...	...
08092375-4735049	08	09	23.75	−47	35	04.9	20.273	M3V	3310	85	19.5	1.8	4.866	0.253	1.317×10^{6}	2.739×10^{5}	0.00	0.00	114.30	0.00	0.0453	0.0089	0.25	...	...

Table 2. *Continued.*

2MASS	RA			DEC			RV	SpT	$T_{\rm eff}$	err	$v \sin i$	err	$EW_{\rm H\alpha}$	err	$F_{\rm H\alpha}$	err	r	err	$10\%W_{\rm H\alpha}$	err	L	err	$M_\star$	$\dot{M}_{\rm acc}^{10\%W}$	$\dot{M}_{\rm acc}^{EW}$	
	hh	mm	ss	°	′	″	(km s^{-1})		(K)		(km s^{-1})		(Å)		(erg cm^{-2}s^{-1})				(km s^{-1})		($L_\odot$)		($M_\odot$)	($M_\odot$ yr^{-1})		
08092398-4744090	08	09	23.98	−47	44	09.0	15.943	M3V	3365	154	11.5	1.6	5.462	0.152	1.685×10^{6}	6.125×10^{5}	0.00	0.00	104.00	4.81	0.0866	0.0214	0.30	...	...	
08092576-4730559	08	09	25.76	−47	30	55.9	17.783	M4V	3292	95	18.0	0.5	2.513	0.118	6.510×10^{5}	1.532×10^{5}	0.00	0.00	105.10	0.00	0.0823	0.0167	0.25	...	...	
08092707-4724277	08	09	27.07	−47	24	27.7	16.269	M3V	3364	154	23.5	1.6	3.387	0.146	1.043×10^{6}	3.807×10^{5}	0.00	0.00	107.40	0.00	0.0572	0.0142	0.30	...	...	
08092749-4723072	08	09	27.49	−47	23	07.2	18.799	M4V	3417	171	55.8	1.8	4.715	0.282	1.319×10^{6}	4.602×10^{5}	0.00	0.00	180.50	0.00	0.0778	0.0203	0.35	...	...	
08092860-4720178	08	09	28.60	−47	20	17.8	14.797	K5V	4406	233	13.6	1.8	1.567	0.102	3.383×10^{6}	1.118×10^{6}	0.00	0.00	121.15	12.94	...	...	...	...	...	
08093012-4657559	08	09	30.12	−46	57	55.9	18.789	K0V	5130	65	31.5	1.8	1.402	0.108	6.599×10^{6}	6.250×10^{5}	0.00	0.00	134.80	0.00	1.1088	0.1932	1.10	...	...	
08093028-4734086	08	09	30.28	−47	34	08.6	16.327	M4V	3374	48	7.7	3.0	6.924	0.175	2.424×10^{6}	2.841×10^{5}	0.00	0.00	112.00	0.00	0.0757	0.0133	0.35	...	...	
08093135-4723124	08	09	31.35	−47	23	12.4	16.922	K8V	3989	63	7.9	1.7	1.362	0.075	1.462×10^{6}	1.931×10^{5}	0.00	0.00	101.70	8.06	0.2361	0.0421	0.85	...	...	
08093154-4737066	08	09	31.54	−47	37	06.6	17.012	M4V	3463	238	15.7	1.6	5.193	0.166	2.003×10^{6}	1.067×10^{6}	0.00	0.00	122.30	8.06	0.1632	0.0525	0.40	...	...	
08093154-4724289	08	09	31.54	−47	24	28.9	20.155	M4V	3418	84	8.5	1.6	4.787	0.223	1.669×10^{6}	3.283×10^{5}	0.00	0.00	113.15	17.75	0.0751	0.0145	0.35	...	...	
08093332-4718502	08	09	33.32	−47	18	50.2	18.045	M1V	3976	106	13.5	1.8	2.675	0.058	2.805×10^{6}	5.644×10^{5}	0.00	0.00	169.15	6.43	...	...	...	...	...	
08093681-4717040	08	09	36.81	−47	17	04.0	16.399	K5V	4254	147	20.9	2.5	2.609	0.205	4.478×10^{6}	1.102×10^{6}	0.00	0.00	148.55	3.18	0.3954	0.0856	1.00	...	...	
08093868-4737070	08	09	38.68	−47	37	07.0	20.333	M4V	3435	184	15.9	1.6	4.992	0.128	1.808×10^{6}	7.548×10^{5}	0.00	0.00	115.45	1.63	0.0798	0.0217	0.40	...	...	
08093920-4721387	08	09	39.20	−47	21	38.7	17.380	K0V	5186	109	21.6	2.9	0.604	0.060	2.978×10^{6}	4.015×10^{5}	0.00	0.00	...	...	1.8452	0.3444	1.30	...	...	
08093936-4739060	08	09	39.36	−47	39	06.0	13.515	M4V	3413	184	20.0	1.8	5.534	0.152	1.901×10^{6}	8.044×10^{5}	0.00	0.00	142.85	8.13	0.1589	0.0433	0.35	...	...	
08094046-4728324	08	09	40.46	−47	28	32.4	20.000	M4V	3288	95	99.7	15.3	6.996	0.217	1.979×10^{6}	4.859×10^{5}	0.00	0.00	377.10	6.51	0.1354	0.0275	0.25	−9.23**	−10.17**	
08094097-4726411	08	09	40.97	−47	26	41.1	18.235	M4V	3356	48	9.6	1.6	8.772	0.153	2.653×10^{6}	2.968×10^{5}	0.00	0.00	107.40	0.00	0.0631	0.0111	0.30	...	...	
08094199-4703317	08	09	41.99	−47	03	31.7	16.992	K8V	4140	186	11.4	2.6	2.563	0.067	3.638×10^{6}	1.179×10^{6}	0.00	0.00	132.55	3.18	0.1527	0.0374	0.75	...	...	
08094478-4720441	08	09	44.78	−47	20	44.1	17.454	K5V	4398	233	33.0	2.5	2.718	0.165	5.801×10^{6}	1.922×10^{6}	0.00	0.00	182.85	12.94	0.6739	0.1817	1.20	...	...	
08094536-4721101	08	09	45.36	−47	21	10.1	15.913	M4V	3259	60	18.0	0.5	10.572	0.247	2.783×10^{6}	4.445×10^{5}	0.10	0.10	132.50	0.00	0.0672	0.0122	0.25	...	...	
08094655-4711042	08	09	46.55	−47	11	04.2	16.102	M4V	3414	184	44.0	2.9	6.512	0.183	2.243×10^{6}	9.480×10^{5}	0.00	0.00	181.70	1.56	0.0837	0.0228	0.35	...	...	
08094692-4731389	08	09	46.92	−47	31	38.9	16.611	M3V	3447	184	12.0	0.5	1.649	0.100	6.138×10^{5}	2.570×10^{5}	0.00	0.00	121.10	0.00	0.1367	0.0370	0.40	...	...	
08094766-4708371	08	09	47.66	−47	08	37.1	14.430	M1V	3975	106	15.0	0.5	2.364	0.099	2.475×10^{6}	5.056×10^{5}	0.00	0.00	126.80	11.31	0.1888	0.0374	0.80	...	...	
08094811-4740323	08	09	48.11	−47	40	32.3	18.886	M4V	3507	92	10.8	1.8	4.569	0.122	1.941×10^{6}	3.910×10^{5}	0.00	0.00	121.15	16.19	0.1046	0.0206	0.45	...	...	
08094852-4719418	08	09	48.52	−47	19	41.8	15.965	M4V	3346	169	14.5	1.6	8.236	0.171	2.433×10^{6}	9.789×10^{5}	0.00	0.00	160.00	0.00	0.1529	0.0400	0.30	...	...	
08094951-4712079	08	09	49.51	−47	12	07.9	19.806	K5V	4452	254	15.5	2.9	2.811	0.124	6.472×10^{6}	2.220×10^{6}	0.00	0.00	132.60	0.00	0.2024	0.0572	0.75	...	...	
08094981-4720129	08	09	49.81	−47	20	12.9	16.754	K1V	4532	443	17.2	2.9	1.295	0.077	3.302×10^{6}	1.835×10^{6}	0.00	0.00	120.00	11.31	0.7097	0.3016	1.15	...	...	
08095048-4723123	08	09	50.48	−47	23	12.3	19.593	M3V	3430	184	19.9	1.8	3.737	0.230	1.337×10^{6}	5.648×10^{5}	0.00	0.00	176.00	0.00	0.1499	0.0407	0.35	...	...	
08095080-4740450	08	09	50.80	−47	40	45.0	19.404	M4V	3360	154	15.9	1.6	3.296	0.166	1.005×10^{6}	3.687×10^{5}	0.00	0.00	102.80	0.00	0.0453	0.0112	0.30	...	...	
08095265-4717121	08	09	52.65	−47	17	12.1	17.617	K5V	4422	146	9.0	2.5	1.057	0.084	2.336×10^{6}	5.049×10^{5}	0.00	0.00	148.60	0.00	0.4333	0.0921	1.00	...	...	
08095370-4716085	08	09	53.70	−47	16	08.5	16.053	M4V	3461	238	34.3	1.8	3.987	0.101	1.531×10^{6}	8.159×10^{5}	0.00	0.00	148.60	0.00	0.2697	0.0868	0.45	...	...	
08095623-4704353	08	09	56.23	−47	04	35.3	17.160	M4V	3417	184	12.0	0.5	4.500	0.083	1.561×10^{6}	6.573×10^{5}	0.00	0.00	116.55	6.43	0.1383	0.0377	0.35	...	...	
08095786-4720085	08	09	57.86	−47	20	08.5	16.935	K5V	4106	76	9.9	3.5	1.446	0.098	1.938×10^{6}	2.888×10^{5}	0.00	0.00	141.70	3.25	0.2924	0.0533	0.95	...	...	
08095807-4737443	08	09	58.07	−47	37	44.3	21.535	M4V	3433	171	27.0	2.7	3.860	0.117	1.115×10^{6}	3.823×10^{5}	0.00	0.00	153.10	0.00	0.1040	0.0270	0.40	...	...	
08095842-4715483	08	09	58.42	−47	15	48.3	16.196	K8V	3881	74	6.9	2.9	3.064	0.136	2.701×10^{6}	3.890×10^{5}	0.00	0.00	116.50	0.00	0.2054	0.0377	0.80	...	...	
08095903-4715230	08	09	59.03	−47	15	23.0	17.141	M1V	3512	270	11.9	3.5	2.488	0.057	1.067×10^{6}	6.287×10^{5}	0.00	0.00	121.10	0.00	0.1759	0.0615	0.45	...	...	
08095922-4716215	08	09	59.22	−47	16	21.5	16.463	K5V	4059	76	6.9	3.5	1.927	0.066	2.373×10^{6}	3.441×10^{5}	0.00	0.00	122.25	14.50	0.2590	0.0473	0.90	...	...	
08095986-4654056	08	09	59.86	−46	54	05.6	18.856	K8V	4013	148	12.0	2.5	2.617	0.245	2.938×10^{6}	8.463×10^{5}	0.00	0.00	129.15	1.63	0.1424	0.0317	0.75	...	...	
08100053-4717581	08	10	00.53	−47	17	58.1	16.559	M4V	3438	184	13.2	2.9	5.515	0.157	2.011×10^{6}	8.388×10^{5}	0.00	0.00	166.80	0.00	0.1351	0.0366	0.40	...	...	
08100066-4744550	08	10	00.66	−47	44	55.0	15.848	M4V	3434	184	14.4	1.8	8.157	0.508	2.947×10^{6}	1.242×10^{6}	0.00	0.00	128.00	0.00	0.1205	0.0327	0.40	...	...	
08100201-4742041	08	10	02.01	−47	42	04.1	20.222	M1V	3853	232	11.3	3.8	2.230	0.069	1.870×10^{6}	8.400×10^{5}	0.00	0.00	118.80	0.00	0.1204	0.0353	0.70	...	...	
08100229-4745123	08	10	02.29	−47	45	12.3	16.275	M3V	3431	184	11.4	1.8	1.611	0.114	5.779×10^{5}	2.448×10^{5}	0.00	0.00	118.90	0.00	0.1304	0.0354	0.40	...	...	
08100280-4736372	08	10	02.80	−47	36	37.2	16.362	M4V	3290	95	16.3	1.8	48.642	0.601	1.382×10^{7}	3.365×10^{6}	0.10	0.10	382.00	2.00	0.0628	0.0127	0.25	−9.18	−8.76	
08100729-4744407	08	10	07.29	−47	44	40.7	16.247	M3V	3436	184	11.4	1.8	3.343	0.151	1.213×10^{6}	5.084×10^{5}	0.00	0.00	134.80	0.00	0.1154	0.0313	0.40	...	...	
08100859-4709118	08	10	08.59	−47	09	11.8	16.032	K8V	3874	74	6.0	2.5	2.382	0.108	2.077×10^{6}	3.004×10^{5}	0.00	0.00	156.55	4.88	0.2372	0.0435	0.85	...	...	
08101040-4730470	08	10	10.40	−47	30	47.0	17.210	K5V	4456	348	15.0	2.5	0.979	0.059	2.266×10^{6}	1.041×10^{6}	0.00	0.00	125.70	0.00	0.6388	0.2262	1.15	...	...	
08101482-4708279	08	10	14.82	−47	08	27.9	16.285	K0V	5129	65	18.0	0.5	0.795	0.071	3.739×10^{6}	3.924×10^{5}	0.00	0.00	...	...	1.0073	0.1755	1.10	...	...	
08101791-4703555	08	10	17.91	−47	03	55.5	16.335	M4V	3351	154	14.6	1.6	4.499	0.110	1.345×10^{6}	4.907×10^{5}	0.00	0.00	116.55	6.43	0.0843	0.0209	0.30	...	...	
08101877-4714065	08	10	18.77	−47	14	06.5	18.856	K8V	*3540*†	200	29.4	1.4	4.856	0.143	2.217×10^{6}	6.717×10^{5}	0.00	0.00	134.80	3.25	0.1598	0.0449	0.50	...	...	
08102227-4727157	08	10	22.27	−47	27	15.7	16.501	K5V	4233	116	8.9	2.5	1.861	0.125	3.086×10^{6}	6.223×10^{5}	0.00	0.00	192.00	13.01	0.3562	0.0711	1.00	...	...	
08102451-4736423	08	10	24.51	−47	36	42.3	16.702	M4V	3347	169	11.0	1.8	4.245	0.132	1.257×10^{6}	5.064×10^{5}	0.00	0.00	134.85	16.19	0.0789	0.0207	0.30	...	...	

† Photometric temperature derived as in Lanzafame et al. (2014).

* Possible accretor.

Table 2. *Continued.*

2MASS	RA			DEC			RV	SpT	$T_{\rm eff}$	err	$v \sin i$	err	$EW_{\rm H\alpha}$	err	$F_{\rm H\alpha}$	err	r	err	$10\%W_{\rm H\alpha}$	err	L	err	$M_\star$	$\dot{M}_{\rm acc}^{10\%W}$	$\dot{M}_{\rm acc}^{EW}$
	hh	mm	ss	°	′	″	(km s^{-1})		(K)		(km s^{-1})		(Å)		(erg cm^{-2}s^{-1})				(km s^{-1})		($L_\odot$)		($M_\odot$)	($M_\odot$ yr^{-1})	
J08103014-4726139	08	10	30.14	−47	26	13.9	16.279	K5V	4396	233	11.0	3.8	2.711	0.202	5.770×10^{6}	1.930×10^{6}	0.00	0.00	221.70	3.25	0.3937	0.1062	1.00	...	...
J08103074-4726219	08	10	30.74	−47	26	21.9	13.633	K5V	4251	152	12.5	2.6	2.221	0.101	3.793×10^{6}	9.331×10^{5}	0.00	0.00	281.05	9.83	0.2753	0.0605	0.90	...	...
J08103418-4657332	08	10	34.18	−46	57	33.2	19.699	K8V	3946	93	9.0	2.2	1.883	0.088	1.872×10^{6}	3.364×10^{5}	0.00	0.00	141.70	3.25	0.3966	0.0759	0.95	...	...
J08103682-4728489	08	10	36.82	−47	28	48.9	15.112	M3V	3440	167	20.0	1.8	2.745	0.066	1.006×10^{6}	3.788×10^{5}	0.00	0.00	124.60	11.31	0.1899	0.0486	0.40	...	...
J08103927-4716476	08	10	39.27	−47	16	47.6	16.674	M4V	3258	60	41.9	4.9	7.442	0.253	1.954×10^{6}	3.158×10^{5}	0.00	0.00	...	...	0.0646	0.0118	0.25	...	...
J08103948-4718465	08	10	39.48	−47	18	46.5	20.976	M3V	3366	154	66.8	5.2	9.379	0.352	2.900×10^{6}	1.056×10^{6}	0.00	0.00	244.50	0.00	0.0567	0.0140	0.30	...	...
J08104075-4734202	08	10	40.75	−47	34	20.2	17.692	M4V	3439	172	17.5	1.6	2.897	0.106	1.059×10^{6}	4.124×10^{5}	0.00	0.00	122.30	11.31	0.1115	0.0290	0.40	...	...
J08104454-4727056	08	10	44.54	−47	27	05.6	17.329	M4V	3383	182	23.0	1.6	5.674	0.198	2.026×10^{6}	8.978×10^{5}	0.00	0.00	161.15	4.88	0.0930	0.0253	0.35	...	...
J08104649-4742216	08	10	46.49	−47	42	21.6	19.299	K8V	3990	93	2.3	3.3	3.401	0.220	3.655×10^{6}	6.903×10^{5}	0.25	0.15	419.60	115.87	0.1913	0.0365	0.80	...	...
J08104745-4703503	08	10	47.45	−47	03	50.3	16.820	M4V	3408	184	36.0	0.5	6.780	0.143	2.301×10^{6}	9.777×10^{5}	0.00	0.00	165.70	11.31	0.1630	0.0445	0.35	...	...
J08104829-4746049	08	10	48.29	−47	46	04.9	17.001	M4V	3445	184	13.1	1.8	4.836	0.189	1.792×10^{6}	7.465×10^{5}	0.00	0.00	138.25	8.13	0.1377	0.0373	0.40	...	...
J08104993-4707477	08	10	49.93	−47	07	47.7	20.000	M4.5V	3285	95	76.0	12.0	10.963	0.342	3.078×10^{6}	7.581×10^{5}	0.25	0.15	304.00	0.00	0.0737	0.0150	0.25	−9.94**	−10.39**
J08105365-4725088	08	10	53.65	−47	25	08.8	11.568	M4V	3340	169	17.5	1.6	6.733	0.120	2.173×10^{6}	9.113×10^{5}	0.00	0.00	163.40	11.31	0.2000	0.0524	0.30	...	...
J08105577-4718066	08	10	55.77	−47	18	06.6	15.035	M4V	3286	95	14.2	1.6	4.892	0.203	1.377×10^{6}	3.409×10^{5}	0.00	0.00	98.30	0.00	0.0588	0.0119	0.25	...	...
J08105600-4740069	08	10	56.00	−47	40	06.9	20.967	M4V	3259	60	15.0	0.5	9.224	0.608	2.428×10^{6}	4.157×10^{5}	0.25	0.15	382.40	4.24	0.0626	0.0114	0.25	−9.18**	−10.57**
J08105880-4718529	08	10	58.80	−47	18	52.9	17.356	M4V	3360	154	11.5	1.6	3.089	0.143	9.423×10^{5}	3.450×10^{5}	0.00	0.00	113.10	11.31	0.0894	0.0222	0.30	...	...
J08110328-4716357	08	11	03.28	−47	16	35.7	13.961	K5V	*3539*†	300	56.3	7.9	6.150	0.279	2.803×10^{6}	1.289×10^{5}	0.00	0.00	334.80	4.81	0.2630	0.0994	0.50	−9.64	−10.04
J08110601-4726209	08	11	06.01	−47	26	20.9	16.151	K8V	3889	75	10.8	1.7	1.926	0.078	1.721×10^{6}	2.482×10^{5}	0.00	0.00	127.95	3.18	0.1573	0.0289	0.75	...	...
J08111144-4727377	08	11	11.44	−47	27	37.7	17.696	K0V	5297	230	22.6	3.5	0.693	0.067	3.744×10^{6}	7.713×10^{5}	0.00	0.00	...	...	1.6940	0.4078	1.15	...	...
J08111185-4729447	08	11	11.85	−47	29	44.7	20.000	M4V	3290	95	114.5	13.5	7.595	0.395	2.158×10^{6}	5.366×10^{5}	0.10	0.10	253.70	0.00	0.1116	0.0226	0.25	...	...
J08111208-4721439	08	11	12.08	−47	21	43.9	17.495	K8V	3888	221	16.9	2.7	3.856	0.161	3.439×10^{6}	1.464×10^{6}	0.00	0.00	136.00	21.07	0.1297	0.0366	0.75	...	...
J08111258-4708072	08	11	12.58	−47	08	07.2	17.542	M4.5V	3285	95	27.0	0.5	8.338	0.352	2.341×10^{6}	5.804×10^{5}	0.00	0.00	141.70	0.00	0.0555	0.0113	0.25	...	...
J08111480-4705207	08	11	14.80	−47	05	20.7	15.849	M4V	3257	60	12.0	0.5	6.734	0.335	1.764×10^{6}	2.922×10^{5}	0.00	0.00	125.70	0.00	0.0608	0.0111	0.25	...	...
J08111784-4723095	08	11	17.84	−47	23	09.5	16.812	M4V	3440	184	13.0	2.9	3.839	0.144	1.406×10^{6}	5.870×10^{5}	0.00	0.00	109.70	3.25	0.1474	0.0400	0.40	...	...
J08112320-4652335	08	11	23.20	−46	52	33.5	19.495	K0V	5130	65	24.0	0.5	1.560	0.098	7.342×10^{6}	6.136×10^{5}	0.00	0.00	129.15	1.63	1.1005	0.1917	1.10	...	...
J08113781-4726376	08	11	37.81	−47	26	37.6	16.381	M4.5V	3285	95	47.4	2.9	7.589	0.219	2.131×10^{6}	5.242×10^{5}	0.10	0.10	182.80	0.00	0.0761	0.0154	0.25	...	...
J08114456-4657516	08	11	44.56	−46	57	51.6	19.358	K5V	*3819*†	250	26.2	1.6	3.599	0.173	2.833×10^{6}	1.437×10^{5}	0.00	0.00	161.10	4.81	0.2475	0.0768	0.80	...	...
J08115579-4731508	08	11	55.79	−47	31	50.8	16.338	M4V	3418	84	9.9	1.6	7.279	0.267	2.532×10^{6}	4.937×10^{5}	0.00	0.00	132.50	0.00	0.0943	0.0182	0.35	...	...
J08115956-4657100	08	11	59.56	−46	57	10.0	16.532	M4V	3356	154	20.5	1.6	4.550	0.254	1.375×10^{6}	5.062×10^{5}	0.00	0.00	137.10	0.00	0.0713	0.0177	0.30	...	...
															UVES										
J08090850-4701407	08	09	08.50	−47	01	40.7	27.893	F1V	6501	141	87.2	4.3	...	...	...	...	0.00	0.00	...	...	5.1911	0.9754	1.50	...	...
J08091875-4708534	08	09	18.75	−47	08	53.4	13.544	F9IV-V	6052	128	40.1	1.6	0.087	0.014	7.812×10^{5}	1.388×10^{5}	0.00	0.00	...	...	1.2186	0.2278	1.20	...	...
J08092627-4731001	08	09	26.27	−47	31	00.1	17.136	K1V	5238	78	31.3	0.8	1.200	0.060	6.179×10^{6}	5.012×10^{5}	0.00	0.00	...	...	1.5230	0.2695	1.20	...	...
J08093304-4737066	08	09	33.04	−47	37	06.6	−28.366	G2V	5614	145	14.1	0.8	0.447	0.054	3.048×10^{6}	4.779×10^{5}	0.00	0.00	...	...	2.5807	0.5070	1.30	...	...
J08094221-4719527	08	09	42.21	−47	19	52.7	50.631	K1V	5087	108	106.5	4.3	2.567	0.118	1.164×10^{7}	1.223×10^{6}	0.00	0.00	...	...	2.0181	0.3775	1.40	...	...
J08095427-4721419	08	09	54.27	−47	21	41.9	21.173	G1.5V	5864	112	19.5	0.7	...	...	...	...	0.00	0.00	...	...	2.4144	0.4427	1.25	...	...
J08095967-4726048	08	09	59.67	−47	26	04.8	...	K0IV	5228	109	175.9	7.1	...	...	...	...	0.00	0.00	...	...	2.2811	0.4251	1.40	...	...
J08110285-4724405	08	11	02.85	−47	24	40.5	16.410	K1V	5137	86	25.4	1.1	0.934	0.076	4.422×10^{6}	4.841×10^{5}	0.00	0.00	...	...	1.0428	0.1873	1.10	...	...

† Photometric temperature derived as in Lanzafame et al. (2014).

* Possible accretor.

Table 3. Parameters of the Cha I members used for this study.

2MASS	RA			DEC			RV	SpT	$T_{\rm eff}$	err	$v \sin i$	err	$EW_{\rm H\alpha}$	err	$F_{\rm H\alpha}$	err	r	err	$10\%W_{\rm H\alpha}$	err	L	err	$M_\star$	$\dot{M}_{\rm acc}^{10\%W}$	$\dot{M}_{\rm acc}^{EW}$
	hh	mm	ss	°	′	″	(km s^{-1})		(K)		(km s^{-1})		(Å)		(erg cm^{2}s^{-1})				(km s^{-1})		($L_\odot$)		($M_\odot$)	($M_\odot$ yr^{-1})	
GIRAFFE																									
0563044-7711393	10	56	30.44	−77	11	39.3	16.234	K5V	4287	108	12.7	2.9	26.954	0.367	4.884×10^{7}	8.316×10^{6}	0.75	0.25	392.92	3.97	0.8070	0.1718	1.30	−9.08	−8.82
0563146-7618334	10	56	31.46	−76	18	33.4	15.068	M4V	3257	60	30.2	2.5	8.943	0.220	2.342×10^{6}	3.746×10^{5}	0.00	0.00	148.36	2.96	0.1719	0.0346	0.25	...	...
0574219-7659356	10	57	42.19	−76	59	35.6	15.784	M4V	3354	154	11.1	1.8	17.774	0.196	5.348×10^{6}	1.948×10^{6}	0.25	0.15	271.90	3.74	0.4711	0.1236	0.45	−10.25**	−9.11**
0575375-7724495	10	57	53.76	−77	24	49.5	15.784	M4V	3298	95	11.4	1.6	3.486	0.191	1.009×10^{6}	2.495×10^{5}	0.00	0.00	132.50	0.00	0.1042	0.0229	0.25	...	...
0590699-7701404	10	59	06.99	−77	01	40.4	17.480	K0IV	5127	65	34.5	1.8	30.115	0.143	1.414×10^{8}	7.841×10^{6}	0.00	0.00	440.93	3.58	4.2824	0.8318	1.60	−8.61	−7.70
1011875-7627025	11	01	18.75	−76	27	02.5	13.245	K8V	4044	150	15.0	0.5	3.367	0.084	4.024×10^{6}	1.090×10^{6}	0.00	0.00	166.80	0.00	0.5866	0.1403	1.10	...	...
1023265-7729129	11	02	32.65	−77	29	12.9	15.153	M4V	3441	184	20.4	1.6	3.726	0.181	1.368×10^{6}	5.724×10^{5}	0.00	0.00	141.70	0.00	0.1516	0.0431	0.40	...	...
1045285-7625514	11	04	52.85	−76	25	51.4	13.594	K8V	3933	74	3.7	3.3	2.823	0.084	2.739×10^{6}	3.776×10^{5}	0.00	0.00	118.80	0.00	0.2904	0.0587	0.90	...	...
1051467-7711290	11	05	14.67	−77	11	29.0	17.170	M4V	3432	217	40.8	54.7	7.144	0.454	1.337×10^{6}	6.701×10^{5}	0.25	0.15	233.35	7.85	0.2173	0.0684	0.40	...	...
1052472-7626209	11	05	24.72	−76	26	20.9	15.098	M4V	3449	184	14.3	1.8	0.000	0.000	0.000×10^{0}	0.000×10^{0}	0.00	0.00	102.80	0.00	0.1137	0.0323	0.40	...	...
1054300-7726517	11	05	43.00	−77	26	51.7	15.470	M4V	3289	95	24.0	0.5	5.550	0.149	1.573×10^{6}	3.852×10^{5}	0.00	0.00	134.80	0.00	0.2172	0.0478	0.30	...	...
1055261-7618255	11	05	52.61	−76	18	25.5	15.000	K5V	4488	285	52.7	1.7	4.961	0.166	1.198×10^{7}	4.432×10^{6}	0.00	0.00	205.70	0.00	0.6810	0.2150	1.15	...	...
1065733-7742106	11	06	57.33	−77	42	10.6	13.005	M3V	3364	154	11.5	1.6	9.433	0.322	2.904×10^{6}	1.057×10^{6}	0.10	0.10	194.08	9.93	0.1503	0.0394	0.35	...	...
1065906-7718535	11	06	59.06	−77	18	53.5	16.000	M4V	3307	85	9.6	1.4	104.700	15.400	3.104×10^{7}	0.802×10^{7}	2.00	0.50	428.81	4.30	0.1608	0.0344	0.30	−8.73	−8.79
1071148-7746394	11	07	11.48	−77	46	39.4	17.064	M1	3887	92	65.0	15.0	4.480	0.274	2.615×10^{6}	1.458×10^{6}	0.00	0.00	212.50	0.00	0.2632	0.0553	0.85	...	...
1071206-7632232	11	07	12.06	−76	32	23.2	16.247	K8V	3952	75	0.0	0.5	15.510	0.227	1.561×10^{7}	2.195×10^{6}	0.30	0.15	526.96	5.29	0.2996	0.0606	0.90	−7.78	−9.67
1071915-7603048	11	07	19.15	−76	03	04.8	14.782	M4V	3570	92	9.5	5.2	15.164	0.351	7.370×10^{6}	1.433×10^{6}	0.50	0.25	370.90	4.40	0.2042	0.0437	0.57	−9.29**	−9.80**
1072022-7738111	11	07	20.22	−77	38	11.1	16.618	M4V	3433	184	22.5	1.8	6.217	0.365	2.241×10^{6}	9.440×10^{5}	0.00	0.00	203.95	20.15	1.685	0.480	0.85	...	...
1072040-7729403	11	07	20.40	−77	29	40.3	14.826	M4V	3289	95	12.0	0.5	4.992	0.115	1.415×10^{6}	3.460×10^{5}	0.00	0.00	112.00	0.00	0.1822	0.0401	0.30	...	...
1072825-7652118	11	07	28.25	−76	52	11.9	15.150	M3V	3361	154	11.0	1.8	27.371	0.449	8.368×10^{6}	3.041×10^{6}	0.50	0.25	330.70	6.67	0.2120	0.0556	0.35	−9.68	−9.34
1074366-7739411	11	07	43.66	−77	39	41.1	15.234	K5V	4149	55	6.8	5.1	64.676	0.506	9.330×10^{7}	8.483×10^{6}	0.50	0.25	355.58	3.58	0.9786	0.1907	1.30	−9.44	−8.27
1075809-7742413	11	07	58.09	−77	42	41.3	19.734	M4V	3388	46	2.3	1.6	64.507	1.010	2.094×10^{7}	2.244×10^{6}	1.25	0.40	502.65	5.04	0.0702	0.0137	0.35	−8.01	−9.73
1080297-7738425	11	08	02.97	−77	38	42.5	17.507	K8V	3985	88	20.4	9.1	65.557	0.719	7.516×10^{7}	2.748×10^{7}	1.50	0.50	432.15	3.65	0.2887	0.0598	0.90	−8.70	−8.97
1081509-7733531	11	08	15.09	−77	33	53.1	14.272	G8III	4938	498	16.5	3.0	6.278	0.239	2.481×10^{7}	1.173×10^{7}	0.00	0.00	380.15	19.48	5.1057	2.2713	1.60	−9.20	−8.31
1081648-7744371	11	08	16.48	−77	44	37.1	15.120	M4V	3371	47	8.5	1.6	3.191	0.093	1.111×10^{6}	1.305×10^{5}	0.00	0.00	112.00	0.00	0.1661	0.0325	0.35	...	...
1083905-7716042	11	08	39.05	−77	16	04.2	13.098	K5V	4467	254	21.7	1.6	55.967	0.670	1.315×10^{8}	4.409×10^{7}	0.10	0.10	471.36	10.76	0.6270	0.1850	1.10	−8.32	−8.54
1084069-7636078	11	08	40.69	−76	36	07.8	12.732	K8V	4017	148	18.5	1.4	4.188	0.135	4.741×10^{6}	1.297×10^{6}	0.00	0.00	269.20	8.77	0.5618	0.1340	1.05	...	...
1085090-7625135	11	08	50.90	−76	25	13.5	13.542	M4V	3292	95	27.0	4.3	22.931	0.631	6.547×10^{6}	1.599×10^{6}	0.10	0.10	318.53	10.75	0.0627	0.0138	0.25	−9.80	−10.13
1085242-7519027	11	08	52.42	−75	19	02.7	13.956	M3V	3368	154	18.9	3.5	3.037	0.110	9.432×10^{5}	3.431×10^{5}	0.50	0.25	272.25	6.86	0.2441	0.0639	0.35	...	...
1085367-7521359	11	08	53.67	−75	21	35.9	14.164	M1V	3685	172	0.0	0.5	54.012	0.667	3.307×10^{7}	1.122×10^{7}	0.50	0.25	377.05	3.78	0.1911	0.0506	0.62	−9.23	−9.28
1085464-7702129	11	08	54.64	−77	02	12.9	15.347	K8V	4140	73	12.7	1.6	13.387	0.368	1.900×10^{7}	2.390×10^{6}	0.50	0.25	413.77	15.48	0.3760	0.0750	1.00	−8.88	−9.60
1090915-7553477	11	09	09.15	−75	53	47.7	13.861	M4V	3455	184	17.2	1.8	1.591	0.147	6.030×10^{5}	2.551×10^{5}	0.00	0.00	121.10	0.00	0.1020	0.0289	0.40	...	...
1091297-7729115	11	09	12.97	−77	29	11.5	13.251	K8V	3876	221	15.8	1.6	5.987	0.150	5.230×10^{6}	2.222×10^{6}	0.00	0.00	132.60	0.00	0.4850	0.1430	0.95	...	...
1091380-7628396	11	09	13.80	−76	28	39.6	13.328	M4V	3260	60	69.0	15.0	6.919	0.263	1.826×10^{6}	2.967×10^{5}	0.00	0.00	205.70	0.00	0.1023	0.0206	0.25	...	...
1094006-7628391	11	09	40.06	−76	28	39.2	15.102	K8V	4042	150	13.8	1.7	3.334	0.138	3.969×10^{6}	1.085×10^{6}	0.00	0.00	146.30	0.00	0.5546	0.1326	1.05	...	...
1095340-7634255	11	09	53.40	−76	34	25.5	10.8*	G9III	4438	157	33.0	6.0	95.448	1.376	2.296×10^{8}	4.226×10^{7}	3.00	0.60	384.28	12.78	2.237	0.5260	1.50	−9.16	−7.51
1095873-7737088	11	09	58.73	−77	37	08.8	14.6*	K8V	3910	31	9.7	1.6	115.398	0.276	7.715×10^{7}	1.724×10^{7}	2.00	0.50	466.99	6.24	0.8552	0.1626	1.05	−8.36	−8.19
1100469-7635452	11	10	04.69	−76	35	45.2	15.513	K5V	4464	254	13.4	1.8	17.073	0.611	3.994×10^{7}	1.351×10^{7}	0.25	0.15	444.55	5.98	0.6503	0.1918	1.15	−8.58	−9.11
1101141-7635292	11	10	11.41	−76	35	29.2	17.073	K5V	4297	117	21.6	1.4	3.850	0.385	7.794×10^{6}	1.424×10^{6}	0.10	0.10	437.10	8.91	1.3670	0.2960	1.40	−8.65**	−8.37**
1101153-7733521	11	10	11.53	−77	33	52.2	13.453	M4V	3261	60	25.3	1.8	4.191	0.185	1.109×10^{6}	1.817×10^{5}	0.00	0.00	123.40	0.00	0.0796	0.0160	0.25	...	...
1102852-7716596	11	10	28.52	−77	16	59.6	15.051	M3V	3257	30	9.6	1.6	5.492	0.195	1.439×10^{6}	1.238×10^{5}	0.00	0.00	98.30	0.00	0.1406	0.0269	0.25	...	...
1104959-7717517	11	10	49.59	−77	17	51.7	15.6*	M4V	3487	43	3.8	1.6	91.346	0.521	3.709×10^{7}	3.562×10^{6}	2.50	0.50	501.49	5.95	0.2585	0.0501	0.45	−8.03	−8.72
1105333-7634319	11	10	53.33	−76	34	31.9	14.5*	M4V	3219	53	4.2	4.1	222.066	0.680	5.258×10^{7}	7.730×10^{6}	2.00	0.50	417.67	1.47	0.1417	0.0282	0.25	−8.84	−8.46
1112260-7705538	11	11	22.60	−77	05	53.8	13.961	M4V	3261	60	18.6	1.6	3.657	0.220	9.677×10^{5}	1.634×10^{5}	0.00	0.00	116.50	0.00	0.1146	0.0231	0.25	...	...
1113474-7636211	11	11	34.74	−76	36	21.1	14.945	K8V	4081	126	15.0	0.5	2.666	0.096	3.417×10^{6}	7.692×10^{5}	0.00	0.00	162.30	0.00	0.3158	0.0709	0.95	...	...
1113965-7620152	11	11	39.65	−76	20	15.2	15.496	M3V	3501	90	0.0	0.5	104.752	0.340	4.379×10^{7}	8.640×10^{6}	2.00	0.50	307.76	3.20	0.4797	0.1026	0.57	−9.90	−8.31
1115400-7619311	11	11	54.00	−76	19	31.1	15.490	K8V	3883	75	5.3	1.6	8.329	0.237	7.371×10^{6}	1.044×10^{6}	0.10	0.10	228.43	5.94	0.6128	0.1243	1.00	...	...
1120984-7634366	11	12	09.84	−76	34	36.6	15.325	M4.5V	3286	95	14.2	1.6	11.649	0.328	3.279×10^{6}	8.055×10^{5}	0.25	0.15	345.03	5.77	0.3011	0.0663	0.30	−9.54**	−9.45**
1122441-7637064	11	12	24.41	−76	37	06.4	15.460	K0V	5131	65	30.6	1.4	3.215	0.135	1.511×10^{7}	1.045×10^{6}	0.00	0.00	383.45	7.14	2.3867	0.4636	1.40	−9.17	−9.18
1124210-7658400	11	12	42.10	−76	58	40.0	15.267	K5V	4456	254	14.3	1.6	1.938	0.130	4.486×10^{6}	1.550×10^{6}	0.00	0.00	...	...	0.4485	0.1324	1.00	...	...
1130450-7534369	11	13	04.50	−75	34	36.9	14.965	M4V	3258	60	23.0	1.6	7.805	0.375	2.050×10^{6}	3.385×10^{5}	0.00	0.00	296.60	9.05	0.1005	0.0202	0.25	...	...

Strongly veiled spectrum. RV measured from the centroid of the Li I λ6707.8 Å line.

Possible accretor.

Table 3. *Continued.*

MASS	RA			DEC			RV	SpT	$T_{\rm eff}$	err	$v \sin i$	err	$EW_{\rm H\alpha}$	err	$F_{\rm H\alpha}$	err	r	err	$10\%W_{\rm H\alpha}$	err	L	err	$M_\star$	$\dot{M}_{\rm acc}^{10\%W}$	$\dot{M}_{\rm acc}^{EW}$
	hh	mm	ss	°	′	″	(km s^{-1})		(K)		(km s^{-1})		(Å)		(erg cm^{-2}s^{-1})				(km s^{-1})		($L_\odot$)		($M_\odot$)	($M_\odot$ yr^{-1})	
1132446-7629227	11	13	24.46	−76	29	22.7	15.347	M4V	3342	30	9.0	0.5	9.512	0.278	3.088×10^{6}	2.482×10^{5}	0.20	0.10	251.07	4.99	0.0860	0.0164	0.30	...	
1132737-7634165	11	13	27.37	−76	34	16.5	13.815	K8V	3867	221	14.9	2.5	3.674	0.111	3.159×10^{6}	1.345×10^{6}	0.00	0.00	162.30	0.00	0.3585	0.1060	0.90	...	
1132970-7629012	11	13	29.71	−76	29	01.2	16.823	M4V	3306	30	9.8	1.6	6.637	0.141	1.968×10^{6}	1.568×10^{5}	0.00	0.00	107.40	0.00	0.1153	0.0220	0.30	...	
1133356-7635374	11	13	33.56	−76	35	37.4	15.772	M4V	3289	95	35.1	2.9	7.722	0.380	2.189×10^{6}	5.436×10^{5}	0.10	0.10	234.65	18.31	0.1148	0.0253	0.25	...	
1141565-7627364	11	14	15.65	−76	27	36.4	16.925	M4V	3292	95	37.3	1.8	6.459	0.161	1.673×10^{6}	3.881×10^{5}	0.00	0.00	189.70	0.00	0.1475	0.0325	0.30	...	
1145031-7733390	11	14	50.31	−77	33	39.0	14.067	M4V	3628	373	15.8	2.9	2.121	0.065	1.161×10^{6}	9.097×10^{5}	0.00	0.00	134.80	0.00	0.3022	0.1366	0.62	...	
1213079-7633351	11	21	30.79	−76	33	35.1	14.653	M4V	3485	238	29.3	1.6	3.498	0.303	1.414×10^{6}	7.547×10^{5}	0.00	0.00	148.60	0.00	0.1985	0.0658	0.45	...	
1242980-7554237	11	24	29.81	−75	54	23.7	10.115	M4V	3291	95	44.0	11.0	5.637	0.128	1.606×10^{6}	3.917×10^{5}	0.00	0.00	162.30	0.00	0.2445	0.0538	0.30	...	
													UVES												
0555973-7724399	10	55	59.73	−77	24	39.9	20.7*	K8V	3640	300	15.0	7.0	39.190	1.156	2.198×10^{7}	1.357×10^{7}	1.00	0.25	415.70	...	0.2356	0.0893	0.62	−8.86	−9.3
0590108-7722407	10	59	01.08	−77	22	40.7	15.172	K8V	4135	125	8.8	0.8	38.336	0.376	5.397×10^{7}	1.186×10^{7}	0.25	0.15	344.60	...	0.6417	0.1432	1.15	−9.55	−8.8
1022491-7733357	11	02	24.91	−77	33	35.7	14.254	K3V	4656	193	14.1	1.2	31.377	0.376	9.265×10^{7}	2.028×10^{7}	0.10	0.10	384.70	...	1.5683	0.3925	1.50	−9.16	−8.8
1045100-7625240	11	04	51.00	−76	25	24.0	13.322	K4V	4571	333	13.8	1.2	2.249	0.126	6.012×10^{6}	2.456×10^{6}	0.00	0.00	...	...	0.6002	0.2080	1.05	...	
1064510-7727023	11	06	45.10	−77	27	02.3	15.967	K5V	4343	147	19.3	2.5	4.604	0.456	9.091×10^{6}	2.197×10^{6}	0.40	0.20	...	...	0.8234	0.1904	1.30	...**	−9.65
1075588-7727257	11	07	55.88	−77	27	25.7	17.591	K3V	4651	174	9.1	1.4	1.336	0.118	3.926×10^{6}	8.546×10^{5}	0.00	0.00	...	...	2.2157	0.5315	1.60	...	
1091172-7729124	11	09	11.72	−77	29	12.4	14.985	M0V	4175	381	5.0	1.6	3.605	0.153	5.412×10^{6}	3.396×10^{6}	0.00	0.00	...	...	0.6123	0.2513	1.15	...	
1091769-7627578	11	09	17.69	−76	27	57.8	15.479	K4V	4524	103	14.8	1.2	1.460	0.096	3.688×10^{6}	5.415×10^{5}	0.00	0.00	...	...	1.0127	0.2111	1.30	...	
1092379-7623207	11	09	23.78	−76	23	20.7	19.9*	M0V	3990	123	7.7	3.0	58.483	0.372	6.282×10^{7}	1.452×10^{7}	2.00	0.50	567.00	...	0.2887	0.0648	0.90	−7.39	−9.0
1100704-7629376	11	10	07.04	−76	29	37.7	13.992	K8V	4697	120	5.1	1.2	50.778	0.452	1.570×10^{8}	2.066×10^{7}	0.10	0.10	450.20	...	1.2300	0.2627	1.40	−8.52	−8.2
1114632-7620092	11	11	46.32	−76	20	09.2	15.911	K3V	4617	207	24.2	1.4	5.188	0.108	1.464×10^{7}	3.534×10^{6}	0.10	0.10	...	...	2.0304	0.5268	1.60	...	−9.6
1124268-7722230	11	12	42.68	−77	22	23.0	14.102	K1V	5239	70	8.6	0.8	1.159	0.064	5.958×10^{6}	4.723×10^{5}	0.00	0.00	...	...	2.8360	0.5529	1.40	...	
1124299-7637049	11	12	42.99	−76	37	04.9	14.250	K3V	4706	220	12.2	0.9	1.269	0.066	3.961×10^{6}	9.779×10^{5}	0.00	0.00	...	...	0.6244	0.1653	1.00	...	
1182024-7621576	11	18	20.24	−76	21	57.6	13.802	K4V	4465	209	8.3	1.2	2.020	0.093	4.732×10^{6}	1.324×10^{6}	0.00	0.00	...	...	0.7767	0.2058	1.20	...	
1291261-7546263	11	29	12.61	−75	46	26.3	15.712	K3V	4818	96	20.8	1.2	1.442	0.099	5.056×10^{6}	6.067×10^{5}	0.00	0.00	...	...	0.9236	0.1882	1.10	...	

Strongly veiled spectrum. RV measured from the centroid of the Li I λ6707.8 Å line.

Possible accretor.

Table 4. Elodie templates.

Name	*SpT*	$T_{\rm eff}$ (K)	$\log g$ (dex)	[Fe/H]
HD338529	F	6239	3.87	-2.34
HD284248	F2	6179	4.39	-1.60
HD216143	G5	4525	1.00	-2.25
HD204543	G0	4650	0.71	-1.86
HD195636	sdG0	5478	3.40	-2.79
HD175305	G5III	4936	2.08	-1.49
HD166161	G5	5272	1.84	-1.25
HD165195	K3p	4058	1.32	-2.72
HD094028	F4V	5747	4.30	-1.62
HD087140	K0	4813	3.01	-2.04
HD064090	sdG2	5083	4.59	-1.94
HD045282	G0w	5044	3.12	-1.65
HD025329	K1V	4632	4.66	-1.72
HD019445	sdG5	5890	4.48	-2.12
HD008724	G5	4711	1.37	-1.65
HD006755	F8V	4970	1.91	-1.66
BD+660268	G0w	5004	4.60	-2.29
BD+233130	G0w	5285	2.83	-2.58
BD+173248	KIIvw	5114	1.03	-2.15
BD+093223	HBstar	5350	1.84	-1.28
BD+044551	F7Vw	5750	3.37	-1.51
BD+023375	F	5960	4.04	-2.34
BD+112998	F8	5425	1.94	-1.25
BD+290366	F8V	5657	4.34	-0.94
HD006833	G9III	4592	1.80	-0.66
HD023439B	K2V	5038	4.49	-0.95
HD025532	F6IV-V	5481	2.00	-1.31
HD064606	K0V	5184	4.52	-0.79
HD078050	G	5033	2.02	-0.94
HD105755	G0Vw	5753	3.88	-0.62
HD148897	G8III	4100	0.09	-1.16
HD159482	G0V	5697	4.09	-0.81
HD194598	F7V-VI	5712	4.33	-1.29
HD201889A	G1V	5634	4.04	-0.78
HD201891	F8V-VI	5659	4.31	-1.21
HD204155	G5	5702	4.01	-0.68
HD233719	K2V	4500	4.49	-0.82
BD+251981	F0	6820	4.11	-1.47
HD003567	G0V-VI	5835	4.02	-1.34
HD046703	F7IVw	6000	0.40	-1.70
HD084937	sdF5	6346	4.00	-2.16
HD142575	F0V	6517	3.72	-1.04
HD195633	G0Vw	6028	3.79	-0.52
HD149143	G0	5936	4.31	0.28
HD182572	G8IV-V	5597	4.18	0.24
HD186155	F5II-III	6637	3.70	0.38
HD001461	G0V	5765	4.38	0.19
HD012661	G6V	5715	4.49	0.23
HD021742	K1IV	5161	4.34	0.08
HD099491	K0IV	5402	4.47	0.23
HD121370	G0IV	6064	3.65	0.24
HD139323	K3V	4922	4.14	0.16
HD154160	G5IV	5352	3.68	0.10
HD211681	G5	5837	4.33	0.44
BD+174708	sdF8	5955	4.00	-1.68
BD+720094	sdF2:	6346	4.48	-1.62
HD000400	F8IV	6136	4.14	-0.26
HD000693	F5V	6171	4.13	-0.33
HD001400	K7Iab:	3967	1.68	-0.10
HD002506	G4III	4917	2.38	-0.55
HD002628	A7III	7161	3.78	-0.24
HD002665	G5IIIwe	4594	2.20	-2.45
HD003229	F5IV	6620	3.86	-0.11
HD003651	K0V	5162	4.43	0.06
HD003883	A7m	7800	3.80	0.53
HD004628	K2V	4985	4.62	-0.33
HD005286	K1IV	4835	3.36	0.08
HD005916	G8III-IV	4953	2.21	-0.72
HD006582	G5Vp	5345	4.43	-0.78
HD007476	F5V	6461	3.99	-0.26
HD008992	F6Ib	6278	1.98	0.11
HD009562	G2IV	5843	4.05	0.15
HD009973	F5Iab	6654	0.99	0.00
HD010380	K3III	4132	2.20	-0.27
HD010476	K1V	5173	4.57	-0.14

Table 4. *Continued.*

Name	*SpT*	$T_{\rm eff}$ (K)	$\log g$ (dex)	[Fe/H]
HD012235	G2IV	6005	4.18	0.21
HD013403	G3V	5576	3.98	-0.35
HD013783	G8V	5493	4.32	-0.54
HD013974	G0V	5721	4.29	-0.44
HD014214	G0.5IV	6062	4.16	0.16
HD017382	K1V	5240	4.49	-0.04
HD019476	K0III	4965	2.90	0.04
HD019994	F8V	6176	4.24	0.21
HD022484	F9IV-V	5964	4.11	-0.07
HD023439	K1V	5000	4.49	-1.07
HD024712	A9Vp	7250	4.30	-0.34
HD025621	F6IV	6301	3.97	0.04
HD026462	F4V	6945	4.14	0.02
HD027022	G5III	5275	2.66	-0.04
HD027348	G8III	5050	3.07	0.11
HD028343	K7V	4284	4.60	0.01
HD029139	K5III	3910	1.59	-0.34
HD030495	G1.5V	5823	4.42	-0.02
HD030562	F8V	5881	4.16	0.19
HD030834	K3III	4115	1.73	-0.21
HD032147	K3V	4381	4.69	0.28
HD033256	F2V	6397	4.00	-0.32
HD033959	A9IV	7670	3.50	-0.14
HD034411	G0V	5888	4.34	0.10
HD037160	G8III	4724	2.72	-0.60
HD037594	A8Vs	7199	4.20	-0.30
HD038309	F0III:n	7149	4.13	-0.10
HD038529	G8III/IV	5552	3.61	0.22
HD038858	G4V	5733	4.49	-0.20
HD039003	K0III	4640	2.61	-0.04
HD040136	F1V	7030	4.20	-0.05
HD041597	G8III	4514	1.74	-0.64
HD045415	G9III	4809	2.67	-0.16
HD045416	K1II	4268	0.62	-0.39
HD045829	K0Iab	4459	0.20	-0.01
HD046122	G3IV	4966	3.09	-0.47
HD048433	K1III	4480	2.15	-0.23
HD048616	F5Ib	6413	3.61	0.40
HD049933	F2V	6570	4.28	-0.44
HD051419	G5V	5637	4.23	-0.35
HD051530	F8V	6032	3.80	-0.42
HD054489	G9III	4542	2.41	-0.21
HD061421	F5IV-V	6485	3.89	0.01
HD062140	A7Vp	7900	4.30	0.50
HD062437	F0III	7873	4.26	-0.03
HD066011	G0IV	6051	3.49	0.18
HD068638	G8V	5518	4.70	-0.23
HD072905	G1.5Vb	5873	4.44	-0.09
HD075318	G5V	5450	4.36	-0.17
HD075732	G8V	5267	4.44	0.29
HD076151	G2V	5788	4.48	0.10
HD082106	K3V	4894	4.55	-0.15
HD085503	K0III	4540	2.20	0.29
HD086728	G1V	5741	4.30	0.18
HD088849	A7m	7402	3.94	0.00
HD089010	G2IV	5622	3.90	0.05
HD095735	M2V	3620	4.90	-0.20
HD102224	K0III	4396	1.56	-0.55
HD106116	G4V	5600	4.39	0.14
HD107168	A8m	8283	4.20	0.39
HD107213	F8V	6274	4.06	0.28
HD113226	G8III	5056	2.85	0.03
HD114710	G0V	6020	4.35	0.07
HD116568	F3V	6605	4.39	0.00
HD117176	G5IV-V	5524	4.01	-0.11
HD117635	G9V	5242	4.30	-0.47
HD120136	F6V	6387	4.26	0.23
HD122120	K5V	4176	4.70	0.28
HD122956	G6IV/Vwl	4600	1.12	-1.78
HD124850	F7IV	6220	3.78	-0.11
HD124897	K1.5III	4249	1.76	-0.61
HD126053	G1.5V	5674	4.49	-0.36
HD126868	G2IV	5697	3.26	0.00
HD127243	G4III-IV	4986	2.38	-0.73
HD128167	F2V	6760	4.36	-0.39

Table 4. *Continued.*

Name	*SpT*	$T_{\rm eff}$ (K)	$\log g$ (dex)	[Fe/H]
HD131977	K4V	4395	4.36	0.07
HD134083	F5V	6435	4.19	-0.02
HD142091	K1IV	4864	3.40	0.09
HD145675	K0V	5261	4.45	0.35
HD146233	G2V	5818	4.45	0.04
HD149661	K0V	5315	4.57	-0.05
HD150177	F7V	6200	3.98	-0.56
HD157214	G2V	5747	4.26	-0.32
HD157881	K7V	4180	4.70	-0.20
HD159181	G2II	5394	1.64	0.00
HD161074	K4III	3980	1.83	-0.27
HD161797	G5IV	5586	3.95	0.20
HD162917	F5V	6380	4.10	0.10
HD165341	K0V	5288	4.57	-0.10
HD165474	A3Vp	9164	4.00	0.42
HD166620	K2V	5000	4.45	-0.26
HD167858	F1V	6982	4.11	0.17
HD168723	K0III-IV	4850	2.96	-0.25
HD169822	G6V	5468	4.30	-0.21
HD173667	F5.5IV-V	6423	3.98	0.03
HD174719	G6V	5520	4.30	-0.27
HD175225	G9IVa	5230	3.55	0.09
HD176737	K4II-III	4123	1.68	-0.10
HD177463	K1III	4572	2.25	-0.26
HD177552	F1V	7025	4.45	-0.03
HD181096	F6IV	6303	3.93	-0.20
HD185144	K0V	5279	4.57	-0.25
HD185758	G1II	5592	2.49	-0.16
HD186379	F8V	5866	3.85	-0.39
HD186408	G1.5V	5773	4.34	0.07
HD186427	G3V	5744	4.26	0.02
HD187691	F8V	6137	4.16	0.16
HD188326	G8IV	5256	3.79	-0.21
HD188512	G9.5IV	5032	3.55	-0.23
HD189558	G1V	5597	3.51	-1.19
HD190007	K4V	4724	4.49	-0.08
HD190228	G5IV	5188	3.65	-0.39
HD190404	K1V	4973	4.64	-0.66
HD191026	K0IV	5096	3.67	-0.04
HD191742	A5p	8842	4.00	1.08
HD194093	F8Ib	6000	1.02	-0.06
HD196502	A2Vp	8842	3.90	0.28
HD196755	G5IV	5640	3.69	-0.02
HD197076	G1V	5778	4.45	-0.10
HD197964	K1IV	4766	3.14	0.07
HD198149	K0IV	4920	3.29	-0.25
HD199960	G1V	5861	4.21	0.20
HD200905	K4Ib...	3920	1.00	-0.41
HD201091	K5V	4361	4.65	-0.19
HD201092	K7V	3932	4.40	-0.29
HD202109	G8III	5030	2.96	-0.02
HD202240	A8II	7560	2.07	-0.13
HD204613	G1IIIwsp	5749	3.83	-0.39
HD204867	G0Ib	5508	1.86	-0.04
HD205512	K0.5III	4638	2.48	-0.10
HD206778	K2Ib	4150	1.25	-0.18
HD206859	G5Ib	4896	1.58	-0.18
HD209750	G2Ib	5230	1.76	-0.07
HD212943	K1III-IV	4609	2.63	-0.32
HD215665	G8II-III	4882	2.15	-0.12
HD216228	K0III	4843	2.75	0.01
HD216385	F7IV	6178	3.85	-0.26
HD217014	G2.5V	5767	4.26	0.15
HD217107	G8IV-V	5623	4.30	0.27
HD219134	K3V	4749	4.40	-0.12
HD219623	F8V	6105	4.18	0.07
HD219877	F3IV-V	6775	4.06	-0.13
HD220954	K0.5III	4658	2.58	-0.06
HD221170	K1IIIw	4520	0.65	-2.11
HD222404	K1IV	4768	3.36	0.11
HD222451	F3V	6632	4.50	0.09
HD223047	G5Ib	4864	1.79	-0.12
HD224930	G5V	5469	4.27	-0.73
HD232078	K3IIp	4000	0.30	-1.54
HD345957	G0Vwe	5548	2.91	-1.70

Table 4. *Continued.*

Name	*SpT*	$T_{\rm eff}$ (K)	$\log g$ (dex)	[Fe/H]
HD132142	K1V	5182	4.53	-0.44
HD010700	G8V	5290	4.43	-0.56
HD000245	G2IV	5722	3.93	-0.59
HD006920	F9IV	5922	3.48	-0.07
HD018768	G1IV	5769	3.68	-0.54
HD043318	F6IV	6196	3.68	-0.21
HD059984	G0IV	5969	3.88	-0.69
HD150680	G1IV	5866	3.72	0.09
HD185351	K0III-IV	5048	3.45	-0.03
HD216219	G2IIIp	5780	3.27	-0.31
HD219916	G8III	5072	3.12	-0.08
HD225239	G2V	5657	3.86	-0.43
HD221377	F7IVw	6275	3.70	-0.82
HD057006	F8IV	6175	3.66	-0.05
HD36395	M0V	4012	4.71	0.35
HD46784	M0III	3616	1.45	0.07
HD79210	M0V	3907	4.61	-0.18
HD79211	M0V	3869	4.71	-0.15
HD42581	M1V	3571	4.6	-0.09
HD119850	M1.5V	3642	4.79	-0.30
BD+442051	M1V	3684	4.9	-0.40
BD+362219	M1V	3451	4.76	-0.21
HD168720	M1III	3790	1.83	0.04
HD169931	M7II	3106	-0.47	-0.21
HD88230	K8V	4085	4.51	-0.16
G 103-68	M4V	3245	4.7	-0.18
HD173739	M3.0V	3407	4.7	-0.49
HD173740	M3.5V	3288	4.93	-0.36
GJ408	M2.5V	3526	4.7	-0.09
GJ2066	M2V	3420	5.0	-0.22
HD1326A	M1.5V	3567	4.5	-0.36
GJ273	M4V	3293	4.8	-0.17
GJ699	M4.5V	3224	5.20	-0.39
GJ166C	M5V	2979	5.0	-0.15
HD175588	M4II	3460	0.14	0.00
HD123657	M4.5III	3506	0.90	-0.03
HD044478	M3III	3667	1.00	-0.09
HD148783	M6III	3250	0.20	-0.01
HD114961	M7III	3014	0.00	-0.81
HD006860	M0III	3800	1.5	-0.04
HD007351	Ms	3600	1.0	0.02
HD017506	K3Ib...	4308	1.00	-0.15
HD018884	M1.5IIIa	3731	0.73	0.02
HD019058	M4II	3500	0.8	-0.15
HD030959	M3s	3452	0.8	-0.15
HD037536	M2Iabs	3789	0.7	-0.15
HD044033	K3Iab:	3950	1.13	0.03
HD089758	M0III	3700	1.35	0.0
HD101153	M4III	3452	0.8	-0.08
HD138481	K5III	3890	1.64	0.2
HD164058	K5III	3900	1.55	-0.08
HD184786	M4.5III	3450	0.5	0.01
HD217906	M2.5II-I	3600	1.2	-0.11
HD225212	K3Iab:	4235	0.80	-0.20
HD039853	K5III	3979	1.23	-0.37
HD049368	S5.1	3700	1.00	-0.45
HD001227	G8II-III	5061	2.97	0.06
HD026162	K2III	4728	2.45	0.09
HD019845	G9III	5050	3.21	0.26
HD027697	K0III	4985	2.73	0.19
HD033419	K0III	4760	2.61	0.19
HD060986	K0III	5124	2.92	0.13
HD042341	K2III	4733	3.1	0.36
HD114357	K2III	4577	2.78	0.25
HD117566	G2.5IIIb	5527	3.17	0.15
HD017361	K1.5III	4672	2.67	0.16
HD007106	K0.5IIIb	4687	2.55	0.08
HD137759	K2III	4539	2.63	0.17
HD008949	K1III	4795	2.86	0.32

Table 5. Hβ equivalent widths and fluxes for the members of γ Vel and Cha I observed with UVES.

2MASS	$EW_{H\beta}$ (Å)	err	$F_{H\beta}$ (erg cm^{-2}s^{-1})	err
		γVel		
J08091875-4708534	0.046	0.011	6.058×10^{5}	1.574×10^{5}
J08092627-4731001	0.373	0.023	2.294×10^{6}	2.422×10^{5}
J08093304-4737066	0.092	0.018	8.303×10^{5}	1.976×10^{5}
J08094221-4719527	0.940	0.084	4.900×10^{6}	7.406×10^{5}
J08110285-4724405	0.185	0.030	1.019×10^{6}	1.915×10^{5}
		Cha I		
J10555973-7724399	2.615	1.994	8.369×10^{5}	9.537×10^{5}
J10590108-7722407	16.623	0.837	1.847×10^{7}	5.259×10^{6}
J11022491-7733357	1.175	0.323	3.430×10^{6}	1.397×10^{6}
J11045100-7625240	1.326	0.208	3.370×10^{6}	1.930×10^{6}
J11064510-7727023	0.032	1.340	5.443×10^{4}	2.279×10^{6}
J11075588-7727257	0.428	0.267	1.268×10^{6}	8.596×10^{5}
J11091172-7729124	3.274	0.266	3.939×10^{6}	3.311×10^{6}
J11091769-7627578	0.570	0.120	1.382×10^{6}	3.744×10^{5}
J11092378-7623207	14.406	0.405	1.124×10^{7}	3.594×10^{6}
J11100704-7629377	8.016	0.468	2.495×10^{7}	4.763×10^{6}
J11114632-7620092	0.970	0.118	2.652×10^{6}	9.384×10^{5}
J11124268-7722230	0.382	0.036	2.368×10^{6}	2.893×10^{5}
J11124299-7637049	0.440	0.057	1.389×10^{6}	4.930×10^{5}
J11182024-7621576	0.986	0.140	2.099×10^{6}	8.310×10^{5}
J11291261-7546263	0.366	0.201	1.354×10^{6}	7.655×10^{5}

Table 6. Mass accretion rates derived in the literature with different methods.

2MASS	$\log \dot{M}_{\rm acc}$ ($M_\odot$ yr^{-1})	Method	Reference
J10555973-7724399	$-7.39^{+0.18}_{-0.17}$	Brγ	(1)
	-8.8 ± 0.3	Hα photometry	(3)
	-8.37 ± 0.6	Spectrophotometry	(7)
	-9.11 ± 0.5	$EW_{\rm H\alpha}$	This work
J10563044-7711393	-8.23 ± 0.6	Spectrophotometry	(7)
	-8.82 ± 0.5	$EW_{\rm H\alpha}$	This work
J10574219-7659356	-8.2 ± 0.1	Hα photometry	(3)
	-8.95 ± 0.5	$EW_{\rm H\alpha}$	This work
J10590699-7701404	-8.06	U-band photometry	(4)
	-7.29 ± 0.5	$EW_{\rm H\alpha}$	This work
J11022491-7733357	-7.92	U-band photometry	(6)
	-7.92	U-band photometry	(4)
	-7.70	Brγ	(5)
	-7.95 ± 0.5	$EW_{\rm H\alpha}$	This work
J11064510-7727023	-8.1 ± 0.2	Hα photometry	(3)
	-9.49 ± 0.5	$EW_{\rm H\alpha}$	This work
J11071915-7603048	-9.82	U-band photometry	(6)
	-9.01	U-band photometry	(4)
	-9.20 ± 0.6	Spectrophotometry	(7)
	-9.69 ± 0.5	$EW_{\rm H\alpha}$	This work
J11072825-7652118	$-9.09^{+0.25}_{-0.83}$	Brγ	(1)
	-7.37 ± 0.6	Spectrophotometry	(7)
	-9.20 ± 0.5	$EW_{\rm H\alpha}$	This work
J11074366-7739411	-8.94 ± 0.6	Spectrophotometry	(7)
	-8.27 ± 0.5	$EW_{\rm H\alpha}$	This work
J11075809-7742413	-8.39 ± 1.11	$EW_{\rm Ca\,II-\lambda8662}$	(2)
	-9.24 ± 0.59	$EW_{\rm H\alpha}$	(2)
	-7.45 ± 2.07	$10\%W_{\rm H\alpha}$	(2)
	-8.14	Brγ	(5)
	-9.60 ± 0.5	$EW_{\rm H\alpha}$	This work
J11080297-7738425	-8.39 ± 0.73	$EW_{\rm Ca\,II-\lambda8662}$	(2)
	-8.65 ± 0.46	$EW_{\rm H\alpha}$	(2)
	-9.14 ± 0.66	$10\%W_{\rm H\alpha}$	(2)
	-8.71 ± 0.5	$EW_{\rm H\alpha}$	This work
J11081509-7733531	-8.09 ± 0.42	$EW_{\rm H\alpha}$	(2)
	-8.68 ± 1.53	$10\%W_{\rm H\alpha}$	(2)
	-8.00 ± 0.5	$EW_{\rm H\alpha}$	This work
J11083905-7716042	-8.92	U-band photometry	(6)
	-8.92	U-band photometry	(4)
	-8.23 ± 0.5	$EW_{\rm H\alpha}$	This work
J11085464-7702129	-8.15	Brγ	(5)
	-9.42 ± 0.5	$EW_{\rm H\alpha}$	This work
J11092379-7623207	-8.28 ± 0.6	Spectrophotometry	(7)
	-9.06 ± 0.5	$EW_{\rm H\alpha}$	This work
J11095340-7634255	-6.5 ± 0.1	Hα photometry	(3)
	-6.85	Brγ	(5)
	-7.0 ± 0.5	$EW_{\rm H\alpha}$	This work
J11095873-7737088	-7.01 ± 0.13	Brγ	(1)
	-7.85 ± 0.68	$EW_{\rm Ca\,II-\lambda8662}$	(2)
	-7.82 ± 0.34	$EW_{\rm H\alpha}$	(2)
	-7.98 ± 0.66	$10\%W_{\rm H\alpha}$	(2)
	-8.47 ± 0.6	Spectrophotometry	(7)
	-7.85 ± 0.5	$EW_{\rm H\alpha}$	This work
J11100469-7635452	-8.9 ± 0.2	Hα photometry	(3)
	-8.87 ± 0.5	$EW_{\rm H\alpha}$	This work
J11100704-7629376	-8.44 ± 0.6	Spectrophotometry	(7)
	-8.24 ± 0.5	$EW_{\rm H\alpha}$	This work
J11101141-7635292	-7.98	Brγ	(5)
	-9.18 ± 0.5	$EW_{\rm H\alpha}$	This work
J11104959-7717517	-7.85	Brγ	(5)
	-8.48 ± 0.5	$EW_{\rm H\alpha}$	This work
J11105333-7634319	-7.90 ± 0.6	Spectrophotometry	(7)
	-8.46 ± 0.5	$EW_{\rm H\alpha}$	This work
J11113965-7620152	-7.81	Brγ	(5)
	-9.07 ± 0.6	Spectrophotometry	(7)
	-8.02 ± 0.5	$EW_{\rm H\alpha}$	This work

Notes: (1): Daemgen et al. (2013); (2): Costigan et al. (2012); (3): Robberto et al. (2012); (4): Espaillat et al. (2011); (5): Antoniucci et al. (2011); (6): Kim et al. (2009); (7): Hartmann et al. (1998).

Appendix A: Cha I: comparing $\dot{M}_{\rm acc}$ with the literature

In Fig. A.1, we compare the mass accretion rates from the literature with those computed in this work from the Hα EW (see also Table 6).

Hartmann et al. (1998) derived mass accretion rates from intermediate-resolution spectrophotometry of the hot continuum emission. Ten accretors are in common with us. Our values and those obtained by these authors are in agreement within the errors with the only exception of J11072825−7652118, for which our $\dot{M}_{\rm acc}$ is lower than the Hartmann et al. (1998) value by ~ 1.7 dex, but it is close to the values reported by other authors (see Daemgen et al. 2013). Three accretors of our sample have been also observed by Kim et al. (2009), who measured $\dot{M}_{\rm acc}$ through U-band photometry. Differences between these values and our determinations are within ~ 0.3 dex, on average. Recently, Espaillat et al. (2011) have measured $\dot{M}_{\rm acc}$ with a similar method like the latter authors; for the four accretors in common with us a mean difference of ~ 0.5 dex is found. Seven accreting objects are in common with Antoniucci et al. (2011), who measured $\dot{M}_{\rm acc}$ through the Brγ line. Four stars show similar mass accretion rates, while the values for the three targets with the lowest $\dot{M}_{\rm acc}$ are higher than ours. Similar differences have been found also by Biazzo et al. (2012) for low-mass stars in Chamaeleon II. Robberto et al. (2012) have derived $\dot{M}_{\rm acc}$ from Hα photometry for five accretors of our sample. The mean difference in $\dot{M}_{\rm acc}$ between their and our value is ~ 0.7 dex. Costigan et al. (2012) report $\dot{M}_{\rm acc}$ measurements using three different diagnostics ($EW_{\rm H\alpha}$, $10\%W_{\rm H\alpha}$, and $EW_{\rm Ca\,II-\lambda8662}$) for four accretors in common with us. The agreement between their results and ours is good, especially when we consider the $\dot{M}_{\rm acc}$ derived from their $EW_{\rm H\alpha}$. The case of J11075809−7742413 is emblematic because they measure the highest difference in $\dot{M}_{\rm acc}$ derived through the three methods, but the value obtained with $EW_{\rm H\alpha}$ is very close to our one. This suggests that the discrepancies in the $\dot{M}_{\rm acc}$ values are mostly due to the method used for deriving it rather than to the different instrumentation used or to an intrinsical variability of the source. Finally, Daemgen et al. (2013) have observed three accretors in common with us and have adopted the Brγ line as diagnostics. The agreement with our values is fairly good, with the exception of 10555973−7724399 for which they have derived $\log \dot{M}_{\rm acc} = -7.4 M_\odot\,{\rm yr}^{-1}$ at odds with our value of $-9.1 M_\odot\,{\rm yr}^{-1}$, which is more similar, within the errors, to the values of $-8.8 M_\odot\,{\rm yr}^{-1}$ and $-8.4 M_\odot\,{\rm yr}^{-1}$ obtained by Robberto et al. (2012) and Hartmann et al. (1998), respectively.

Concluding, we think that the comparison between our $\dot{M}_{\rm acc}$, as derived from the Hα luminosity, and the literature values is in general quite good. The differences/inconsistencies can be attributed to intrinsic short-term and long-term variability (as outlined in Sect. 4.4) and the different photometric/spectroscopic methodologies used by each author to derive accretion luminosity and mass accretion rate, as well as to the different evolutionary models adopted to estimate the stellar parameters (as also recently pointed out by Alcalá et al. 2014).

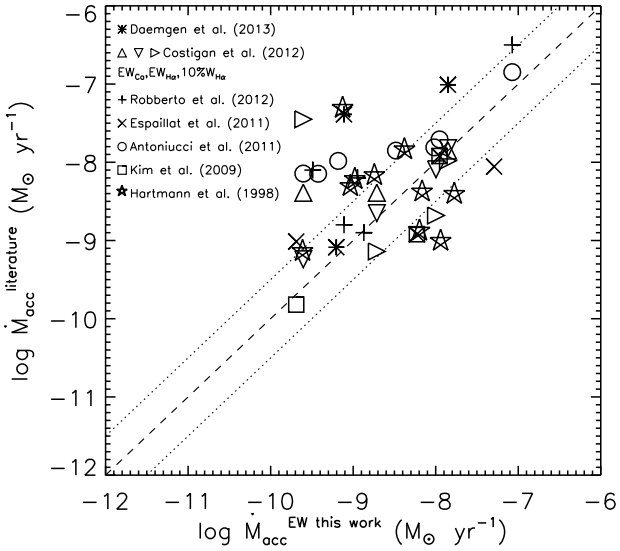

Fig. A.1. Comparison between our $\dot{M}_{\rm acc}$ values calculated using the $EW_{\rm H\alpha}$ and those obtained by several authors. Dashed and dotted lines represent the one-to-one relation and the position of the typical mean error in $\dot{M}_{\rm acc}$ of ± 0.5 dex. The legend in the upper left corner explains the meaning of the symbols.